Astronomy & Astrophysics manuscript no. 37885corr˙auth2 May 25, 2020
(DOI: will be inserted by hand later)

Sunquake with a second bounce, other sunquakes, and emission associated with the X9.3 flare of 6 September 2017. II. Proposed interpretation

Valentina Zharkova[1], Sergei Zharkov[2], Malcolm Druett[3], Sarah Matthews[4], and Satoshi Inoue[5]

[1] Northumbria University, Department of Mathematics, Physics and Electrical Engineering, Newcastle upon Tyne, NE1 8ST, United Kingdom
[2] E.A.Milne Centre for Astrophysics, School of Mathematics and Physical Sciences, Hull University, Kingston upon Hull, HU6 7RX, United Kingdom
[3] Stockholm University, Department of Astronomy, SE-106 91 Stockholm, Sweden,
[4] UCL Mullard Space Science Laboratory, Holmbury St. Mary, Dorking, Surrey, RH5 6NT, United Kingdom
[5] Institute for Space–Earth Environmental Research (ISEE), Nagoya University, Furo-cho, Chikusa-ku, Nagoya, Japan, 464 8601

May 25, 2020

Abstract. In this paper we present the interpretation of the observations of the flare from 6 September 2017 reported in Paper 1. These include gamma-ray (GR), hard X-ray (HXR), soft X-rays (SXR), Lyα line, extreme ultraviolet (EUV), Hα, and white light (WL) emission, which were recorded during the two flaring events 1 (FE1) and 2 (FE2) that occurred at 11:55:37 UT (FE1) and 12:06:40 UT (FE2). Paper 1 also reported the first detection of the sunquake with first and second bounces of seismic waves combined with four other sunquakes in different locations supported with the observations of HXR, GR, EUV, Hα, and WL emission with strongly varying spatial resolution and temporal coverage. In the current Paper 2, we propose some likely scenarios for heating of flaring atmospheres in the footpoints with sunquakes which were supported with EUV and Hα emission. We used a range of parameters derived from the HXR, EUV, and Hα line observations to generate hydrodynamic models, which can account for the blueshifts derived from the EUV emission and the redshifts observed with the EUV Imaging Spectrometer (EIS) in the He II line and by the CRisp Imaging Spectro-Polarimeter (CRISP) in the Swedish Solar Telescope (SST) in Hα line emission. The parameters of hydrodynamic shocks produced by different beams in flaring atmospheres were used as the initial conditions for another type of hydrodynamic models that were developed for acoustic wave propagation in the solar interior. These models simulate the sets of acoustic waves produced in the interior by the hydrodynamic shocks from atmospheres above deposited in different footpoints of magnetic loops. The Hα line profiles with large redshifts in three kernels (two in FE1 and one in FE2) were interpreted with the full non-local thermodynamic equilibrium (NLTE) radiative simulations in all optically thick transitions (Lyman lines and continuum Hα, Hβ, and Pα) applied for flaring atmospheres with fast downward motions while considering thermal and non-thermal excitation and ionisation of hydrogen atoms by energetic power-law electron beams. The observed Hα line profiles in three kernels were fit with the simulate blue wing emission of the Hα line profiles shifted significantly (by 4-6 Å) towards the line red wings, because of strong downward motions with velocities about 300 km/s by the shocks generated in flaring atmospheres by powerful beams. The flaring atmosphere associated with the largest sunquake (seismic source 2 in FE1) is found consistent with being induced by a strong hydrodynamic shock produced by a mixed beam deposited at an angle of -30° from the local vertical. We explain the occurrence of a second bounce in the largest sunquake by a stronger momentum delivered by the shock generated in the flaring atmosphere by a mixed beam and deeper depths of the interior where this shock was deposited. Indeed, the shock with mixed beam parameters is found deposited deeply into the interior beneath the flaring atmosphere under the angle to the local vertical that would allow the acoustic waves generated in the direction closer to the surface to conserve enough energy for the second bounces from the interior layers and from the photosphere. The wave characteristics of seismic sources 1 and 3 (in FE1) were consistent with those produced by the shocks generated by similar mixed beams deposited at the angles -(0 – 10)° (seismic source 1) and +30° (seismic source 3) to the local vertical. The differences of seismic signatures produced in the flares of 6 September 2011 and 2017 are also discussed.

Key words. Sun: flares, Sun: X-rays, gamma-rays, Sun: helioseismology, radiative transfer, hydrodynamics

Send offprint requests to: v.zharkova e-mail: valentina.zharkova@northumbria.ac.uk

1. Introduction

On the 6 September 2017, the active region NOAA 12673 produced two X-class flares: an X2.2 flare and, three hours

later, an X9.3 flare which have been studied by many authors. A few sunquakes and magneto-acoustic waves associated with the X9.3 flare were reported previously (Sharykin & Kosovichev 2018; Zhao & Chen 2018). The X9.3 flare from 6 September 2017 is explored in part 1 of our research (Zharkov et al. 2020, hereafter Paper 1), which presents the available observations of gamma-ray (GR), hard X-ray (HXR), extreme ultraviolet (EUV), Hα, and white light emission combined with four (possibly five) sunquakes detected by the Helioseismic and Magnetic Imager (HMI) aboard the Solar Dynamic Observatory (SDO) (Scherrer et al. 2012) in the footpoints of three magnetic flux ropes as shown from the investigation of magnetic field associated with this flare (Inoue et al. 2018). In Paper 1 pertaining to the investigation of this flare observations (Zharkov et al. 2020), we present, for the first time, a detection of the largest sunquake with the first and second bounces of acoustic waves generated in the solar interior. Another three, or potentially four, sunquakes were also detected in other with rather different characteristics. In the current paper, we compare the physical conditions in flaring atmospheres, leading to sunquakes that are generated around given footpoints of magnetic flux ropes that are restored with the non-linear force-free field (NLFFF) extrapolation of the magnetic field in this active region prior to the flare onset followed by 3-dimensional (3D) magneto-hydrodynamic (MHD) simulations of the magnetic structures, which led to the flare on 6 September 2017 (Inoue et al. 2018).

The X9.3 flare was observed with the Gamma Ray Burst Detector (KONUS) payload (Lysenko et al. 2019) aboard the WIND satellite (Aptekar et al. 1995), with Lyα light curves by the Large-Yield RAdiometer (LYRA) instrument on board of the PROBA 2 satellite (Hochedez et al. 2006; Dominique et al. 2013), showing four flaring events (FEs), from which we analysed FE1 and FE2 (see for details Zharkov et al. 2020). There were also observations with the Reuven Ramaty High Energy Solar Spectroscopic Imager (RHESSI) (Lin et al. 2002), which occurred 1.2 minutes after FE2. Since neither the KONUS/WIND or LYRA data have any spatial resolution and as the HXR observations by RHESSI were not available for FE1 or FE2, they thus cannot be used directly for the beam parameter definition. Hence, for this flare we are left with Hα emission locations which were observed with the CRisp Imaging Spectro-Polarimeter (CRISP) (Scharmer et al. 2003; Scharmer 2006) at the Swedish Solar Telescope (SST) to distinguish the areas of the footpoints where heating by the beams has occurred that can provide us with some guidance about a range of the parameters of particle beams generating these signatures.

In Paper 1 (Zharkov et al. 2020), the parameters flaring atmospheres in few locations were derived from the EUV observations with the EUV Imaging Spectrometer (EIS) on Hinode spacecraft (Culhane et al. 2007) in the spectrograms for the Fe XXIII 263.76 Å line profiles for large blueshifts and He II 256 Å line profiles, revealing redshifts during the impulsive phase that are later followed by blueshifts at the gradual phase when the flaring plasma starts returning to the pre-flare status. For the dynamics of the lower atmosphere in flaring events 1 and 2, we explored from Hα line profile observations by the CRISP/SST instrument in two Hα kernels for FE1 that is linked to seismic sources 1 and 2 and one Hα kernel 3 in FE2 that is seen 10 minutes later in the same location as seismic source 2. The Hα line profiles in each location indicate the observation of blue wings of the profiles, while the core is strongly redshifted well beyond the spectral window of ±1.5Å for the CRISP/SST. Moreover, the SST observations in the available wavelength range are consistent with the previous observations of hydrogen Hα line emission, often revealing cores with large redshifts up to 5 Å (Ichimoto & Kurokawa 1984; Canfield & Gayley 1987; Zarro et al. 1988; Wuelser & Marti 1989).

In addition, there was an increase in white light (WL) (Paschen continuum) in this flare, similarly to many other flaring events (Uchida & Hudson 1972; Kurokawa et al. 1988; Matthews et al. 2011) and Balmer continuum emission (Kotrč et al. 2016), which are nearly co-spatial with the HXR emission. Uchida & Hudson (1972) suggested that a sharp increase of continuous emission in flares is caused by energetic electron beams that are injected into a flaring atmosphere. Recently, Druett et al. (2017) and Druett & Zharkova (2018) have shown that non-thermal ionisation of hydrogen atoms by relativistic electron beams can naturally bf produce during flares strong increases in the Balmer near UV and Paschen WL emissions at the chromospheric levels, in addition to photospheric depths, these beams can produce the profiles of Hα lines that are strongly (by 3-5 Å) shifted to the red wings, leaving only blue wings of the line observations (Druett & Zharkova 2018) if they are carried out with a narrow spectral filter of ± 1.5 Å.

The high-energy emissions in HXR, EUV, UV, and optical wavelengths are often accompanied by the occurrence of sunquakes or ripples on the solar surface that radially emanates from a point source from 20-60 minutes after a flare onset (Kosovichev & Zharkova 1998; Zharkova 2008; Donea 2011; Zharkov et al. 2011a; Zharkov et al. 2011b; Matthews et al. 2015). Sunquakes are detected on the solar surface using time-distance (TD) diagram analysis (Kosovichev & Zharkova 1998; Zharkov et al. 2011a; Zharkov et al. 2011b) and acoustic holography (Donea et al. 1999; Lindsey & Braun 1999; Donea et al. 2000; Lindsey & Braun 2000; Donea & Lindsey 2005; Zharkov et al. 2011a). The sunquake origin is normally indicated by a compact bright kernel (source) that peaks during a flare, which is verified by statistical tests (Zharkov et al. 2011a). Some localised magnetic configurations are found to be more effective in channelling the energy and momentum to the lower atmosphere (Green et al. 2017).

The ripples were suggested to be the reflections from the solar surface of acoustic (in some cases, magneto-acoustic) waves induced by a sharp deposition into the solar interior of the momentum that was delivered by hydrodynamic shocks that formed in flaring atmospheres by hydrodynamic responses to the injection of particle beams (Somov et al. 1981; Fisher et al. 1985b,a; Allred et al. 2005; Zharkova & Zharkov 2007; Zharkova & Zharkov 2015) and travelling with supersonic speeds downwards to photospheric levels and the solar interior (Kosovichev & Zharkova 1998; Zharkov 2013). The other authors explored radiative back-warming as the other source of pressure transients producing acoustic waves in flares (Donea et al. 2006; Donea 2011). However, the observations showed

that nearly half of sunquake locations are associated with little or no white light emission (Matthews et al. 2011; Buitrago-Casas et al. 2015; Zharkov et al. 2011a), thus ruling out this mechanism as the main cause. And the third mechanism for the generation of sunquakes can occur in the locations of Lorentz force transients, which, supposedly, can produce a well-directed magnetic impulse of Poynting vector towards the photosphere and subsequent magneto-acoustic waves (Hudson et al. 2008; Fisher et al. 2012).

Recently, Macrae et al. (2018) detected a missing sunquake in the flare of 6 September 2011 in a previously not acoustically active flare (Liu et al. 2014); and they provided the first quantitative interpretation of the sunquake's properties (timing, directionality) using a hydrodynamic response to plasma heating by beam electrons as an input for the another hydrodynamic model for acoustic wave propagation in the solar interior. They demonstrate that, in fact, all three mechanisms associated with the generation of seismic signatures, are present in flaring atmospheres when they have sunquakes. The energetic particles are likely to gain their energy from reconnecting current sheets of flares by converting the magnetic energy into energetic particles with the help of the Lorentz force. Then these relativistic electrons can over-ionise the ambient hydrogen plasmas by 5-6 orders of magnitude and keep this ionisation for up to 40 minutes by radiative transfer in optically-thick Lyman continuum (Druett & Zharkova 2019), which leads to appearance of Balmer continuum emission and white light emission in Paschen continuum (Druett & Zharkova 2018). While the hydrodynamic shocks produced by hydrodynamic responses of flaring atmospheres to heating by energetic particles generate acoustic waves in the solar interior, which are observed on the solar surface as ripples, or sunquakes.

Energetic particles accelerated in current sheets occurring on the top of flaring atmospheres (Zharkova et al. 2011) are found to deliver their energy to deeper layers of a flaring atmosphere causing its heating. During the impulsive phase of flares, the injected particle beams are shown to precipitate into flaring atmospheres and heat them via Coulomb collisions (Brown 1971; Syrovatskii & Shmeleva 1972), causing hydrodynamic responses of flaring atmospheres (Somov et al. 1981; Fisher et al. 1985b; Allred et al. 2005; Zharkova & Zharkov 2007; Zharkova & Zharkov 2015). In type one hydrodynamic models of flaring atmospheres, the intense heating by particle beams of the quiet Sun (QS) chromosphere is shown to sweep the ambient plasma to a lower atmosphere, forming a new flaring atmosphere with its own corona, transition region and chromosphere (Somov et al. 1981; Duijveman et al. 1983; Zharkova & Zharkov 2007). This sweeping of chromospheric plasma by precipitating beams is quickly followed by evaporation of this plasma back to the corona combined with strong hydrodynamic shocks propagating with supersonic speeds downwards to the photosphere and beneath it (Somov et al. 1981; Fisher et al. 1985c,b,a; Allred et al. 2005; Zharkova & Zharkov 2007; Zharkova & Zharkov 2015).

This hydrodynamic response of ambient plasmas heated by very intense beams injected for only 5-10 seconds causes a formation of the new flaring atmosphere with a sharp increase of its temperature, a decrease of the ambient density in the corona combined with hydrodynamic shocks formed in the chromosphere, and strong macro-motion upwards and downwards that is associated with the explosive evaporation of the chromospheric plasma into a flaring corona and propagations of hydrodynamic shocks towards the solar interior (Somov et al. 1981; Duijveman et al. 1983; Fisher et al. 1985b; Zharkova & Zharkov 2007; Zharkova & Zharkov 2015). There are two other models of hydrodynamic heating (in preheated atmospheres or isotropic heating), which produce much milder chromospheric plasma evaporation without sweeping, combined with the shocks moving with much smaller velocities downwards to the lower atmosphere (Polito et al. 2016; Fisher et al. 1985c,b; Allred et al. 2005; Kennedy et al. 2015; Bradshaw & Cargill 2006). These models are not relevant for the atmospheres with large redshifted line emission and sunquakes requiring a very strong moment deposition to a lower atmosphere and solar interior to produce the ripples (Kosovichev & Zharkova 1998; Zharkova 2008; Donea 2011; Zharkova & Zharkov 2015).

In this paper, we consider flaring atmospheres heated by short pulses of powerful particle beams, which keep them heated for rather long periods of time lasting 1-1.5 hours after the beam offset before they are fully cooled off to pre-flare conditions (Somov et al. 1981; Duijveman et al. 1983; Fisher et al. 1985b; Zharkova & Zharkov 2007). These shocks subsequently travel with supersonic speeds for about 40-50 seconds towards the flaring photosphere and the interior beneath (Macrae et al. 2018). The HD shocks are shown to induce acoustic (and magneto-acoustic) waves in the solar interior, which are seen as ripples on the solar surface, or sunquakes (Zharkov 2013). The shock speed profile for the 6 September 2011 flare was evaluated from the simulations and it was compared with the sound speed expected in the solar interior. This helped to define the key characteristics of the acoustic waves that have formed in the solar interior by this shock, thus producing the first successful quantitative interpretation of the simultaneous seismic and optical signatures recorded for this flare from 6 September 2011 (Macrae et al. 2018).

In addition, it was shown (Zharkova & Kobylinskii 1993) that electron beams can cause essential non-thermal collisional ionisation and excitation of hydrogen atoms by beam electrons that strongly (by a few orders of magnitude) increase the excitation and ionisation degree of hydrogen atoms from all atomic levels. The non-thermal collisions and ionisation combined with plasma heating caused by beam electrons can lead to an increase in hydrogen line and continuum radiation in a Lyman, Balmer, and Paschen series that was recently verified with the detailed radiative hydrodynamic simulations using the HYDRO2GEN code (Druett et al. 2017; Druett & Zharkova 2018, 2019). The authors confirm the enhancement of Lyman, Balmer, and Paschen lines and continua of hydrogen atoms in flares caused by beam electrons. Druett & Zharkova (2019) show that after the beam is switched off, the high ionisation degree of a flaring plasma, gained during the beam injection, is sustained for a very long time by Lyman continuum emission because of its large opacity. This leads to a long enhancement of hydrogen ionisation in flaring atmospheres and an increase of Lyman -α and β line emission in the line cores and wings (Druett & Zharkova 2019).

Using the radiative hydrodynamic model HYDRO2GEN allowed us to naturally explain the earlier wide-spectral filter Hα line observations with large (2-5 Å) redshifts (e.g. Ichimoto & Kurokawa 1984; Wuelser & Marti 1989) by the propagation of hydrodynamic shocks that formed in flaring atmospheres as the result of the injection of electron beams (Druett et al. 2017; Druett & Zharkova 2018). However, these large redshifts cannot be seen by modern instruments with narrow (±1.5Å) spectral windows (Druett et al. 2017; Druett & Zharkova 2018) that explains the frequently reported delays of the order of 30 s for the appearance of Hα-line emission with respect to HXR emission in powerful flares (Kaempfer & Magun 1983; Veronig et al. 2002; Radziszewski et al. 2011). Moreover, the simulations with the HYDRO2GEN code also accounted for the close timing and locations of HXR and WL emissions seen in the solar flares on the limb (Martínez-Oliveros et al. 2012), indicating the very close heights and timing of formation of these emissions in flaring atmospheres that was interpreted by the increased non-thermal ionisation of hydrogen atoms by beam electrons (Druett & Zharkova 2018), maintained by radiative transfer in the Lyman continuum (Druett & Zharkova 2019).

In the current paper, we use the properties of flaring atmospheres that are heated by particle beams, which are linked to detected Hα kernels and sunquakes in the 6 September 2017 flare, and simulate the hydrodynamic responses of these atmospheres to the injection of particle beams whose physical parameters can be tested with the observed EUV, Hα, white light, and seismic signatures. These simulations were extended to the investigation of the production of seismic waves by using the hydrodynamic shocks that were generated in flaring atmospheres (HD models 1) as the initial condition for the hydrodynamic models 2, which were applied for the generation of acoustic waves in the solar interior. This approach allows us to obtain the sets of acoustic waves in the interior and to detect their first bounces from the solar surface, or ripples, observed as sunquakes in the vicinity of these flaring atmospheres.

The hydrodynamic model 1 of flaring atmospheres heated by particle beams are discussed in Section 2. The hydrodynamic shocks and their role in formation of hydrogen Hα emission with large redshifts and white light emission are discussed in Section 3. The hydrodynamic models of acoustic wave formation in the solar interior are explored in Section 4, and a general discussion of the results and conclusions are drawn in Section 5.

2. Hydrodynamic heating of flaring atmospheres

The plasma of a flaring atmosphere is heated by the injection of particle beams, which are injected into the QS chromosphere from the primary energy release point in the corona, and precipitate from the top boundary with the heating function derived from the flux conservation equation (Brown 1971), the continuity equation (Syrovatskii & Shmeleva 1972), or the Fokker-Planck equation (Gordovskyy et al. 2005; Siversky & Zharkova 2009). The beam electrons are assumed to heat the cold ambient chromospheric plasma, sweeping it as a piston to deeper atmospheric levels (Syrovatskii & Shmeleva 1972). This heating prompts a hydrodynamic response of the ambient plasma, thus turning the QS chromosphere into a flaring atmosphere (Somov et al. 1981; Zharkova & Zharkov 2007).

2.1. Brief summary of the detected flaring events

The X9.3 flare on the 6 September 2017 started at 11:55:37 UT at the solar disc location S09W34 and comprised two flaring events: flaring event 1 (FE1) starting at 11:55:37 UT and flaring event 2 (FE2) starting at 12:06:40 UT, which are described in Paper 1 (Zharkov et al. 2020). The non-linear force-free field (NLFFF) restoration of the magnetic field in the active region 12673 prior to the X2.2 flare followed by 3D MHD simulations of magnetic field dynamics during the two solar flaring events of X-class, occurring on 6 September 2017 (Inoue et al. 2018), revealed that after the X2.2 flare and prior to the X9.3 flare that three magnetic flux ropes (MFRs) formed with very braided and twisted magnetic structures as shown in Fig. 1a. The places where the three magnetic flux ropes are embedded into the photosphere, or the rope footpoints referred to as F1-F6, are close to the locations of the four sunquakes shown in Fig. 1b as detected in Paper 1.

We intend to explore physical conditions in the flux ropes, which produced four (possibly five) seismic sources; the locations of which are indicated by the asterisks in the HMI white light image in Fig. 1b. The asterisks indicate the locations, from which the time-distance diagrams of sunquakes (seismic sources 1-3) or holography sources (1-4) were obtained. The Hα kernels 1 and 2 were detected in the locations of seismic sources 1 and 2 in flaring event 1. Additionally, Hα kernel 3 was detected in the same location as seismic source 2, but during the flaring event 2, when we suggest the potential seismic source 5 is likely to occur.

2.2. Heating by particle beams

This flare had at least four flaring events detected in Ly α line emission, which were observed without spatial resolution by GOES and LYRA instruments with soft X-ray (SXR) and Lyman-α light curves, indicating the times for each event (Hochedez et al. 2006; Dominique et al. 2013). From these flaring events, we investigated two events FE1 and FE2. For FE1, we have high energy HXR and gamma-ray (GR) observations by the KONUS/WIND payload without any spatial resolution (FE1)(Lysenko et al. 2019). There were no HXR observations for FE2. The only HXR observations by the RHESSI payload (spatial resolution 2") were obtained more than one minute after the FE2 onset. Hence, we had to use the areas on Hα kernels to account for the areas of footpoints where particle beams precipitate and produce HXR emission reported by the KONUS payload. Then we linked these Hα kernels by times of occurrences and locations to the locations detected sunquake 1 (SQ1), sunquake 2 (SQ2), and sunquake 3 (SQ3) for FE1 and hypothetical SQ 5 for FE2.

Thus, in order to derive the specific conditions in the atmospheres leading to the observed seismic sources 1-3, which are associated with FE1, we involved Hα kernels observed with

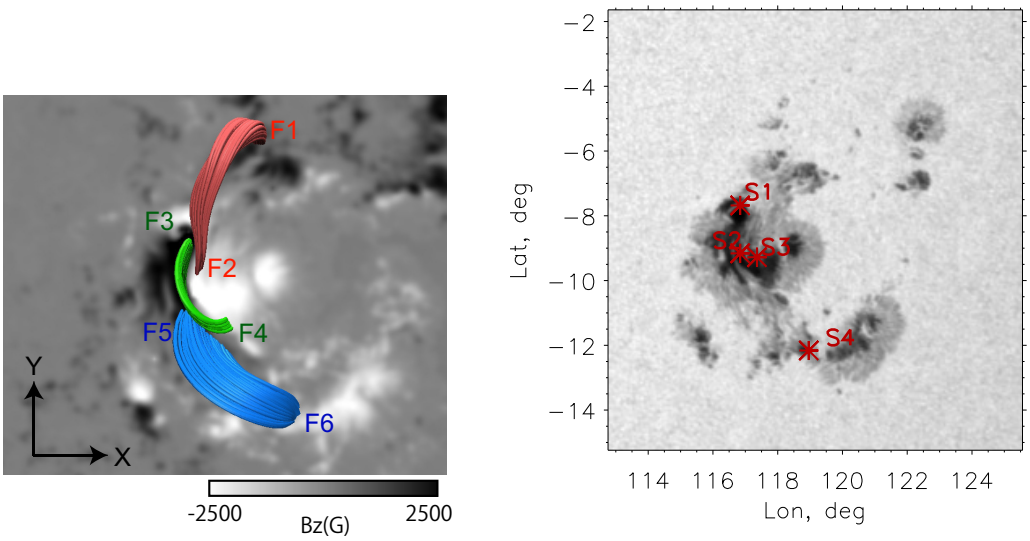

(a) Three magnetic ropes

(b) Seismic sources S1-S4

Fig. 1. Magnetic flux ropes formed prior to the 9.3X flare of 6 September 2017 derived from NLFFF magnetic field reconstruction and MHD simulations by Inoue et al. (2018). (a) The locations of four sunquakes detected for the flare (b) adopted from Paper 1.

high spatial resolution (0.06") by the CRISP/SST instrument, giving us the areas of the footpoints and characteristics of the seismic sources themselves. Based on the observations during the flaring event 1 when three seismic sources were detected with strong HXR and GR emission (both continuous and nuclear lines) by the KONUS payload without any spatial resolution (Lysenko et al. 2019), which indicates the presence of electrons as well as protons and ions that heat the flaring atmospheres, we need to consider the mixed beams that are injected into these footpoints with an equal proportion of electrons (50%) and protons (50%), in the absence of any tools to assume otherwise, which can produce the overall HXR and GR emission observed at this event.

We used the averaged in time HXR energy spectrum, which was derived from the KONUS instrument, from which we derived the averaged spectral index of four and the total power of the beam of about $1.1 \cdot 10^{31}$ erg (see discussion in Lysenko et al. 2019, p.11). Moreover, in the discussion of their paper Lysenko et al. (2019) report that during the initial impulsive phase, the lower energy part of the HXR spectrum revealed the soft-hard-soft (SHS) pattern, indicating that the beam heats the flaring atmospheres in this event. We conclude that this beam had to have a large initial energy flux, increasing and decreasing in time as a triangle function following the kinetic Fokker-Planck solutions (Zharkova & Gordovskyy 2006), indicating that the SHS pattern in HXR energy spectrum has a presence of strong return currents if the beam energy flux becomes much higher than $1 \cdot 10^{11}\ erg \cdot cm^{-2} s^{-1}$.

Flaring event 1 was induced by the mixed beam with a total energy of $1.2 \cdot 10^{31}$ erg by using the observed areas of Hα line kernels 1 and 2, by assuming that the area of the footpoint for the Hα kernel 3 was similar to that in kernel 2, and by looking at the shapes of Hα line profiles, or their blue wings, seen in all three kernels, as derived in Paper 1 (Zharkov et al. 2020), the initial energy flux of the beam to vary between $(8 - 12) \cdot 10^{12}$ $erg \cdot cm^{-2} s^{-1}$ depending on the area of a particular kernel or seismic source. In the absence of other options, we still can use a spectral index of 4 for these beams which were derived from the KONUS observations.

Due to the fact that the very strong sunquake 2 was detected in kernel 2 in footpoint F4 (southern footpoint of the green rope) indicating a strong shock and using our previous simulations of Hα line profiles affected by strong shocks (Druett et al. 2017; Druett & Zharkova 2018), it looks very likely that a very intense mixed beam was injected into this footpoint, where protons can deliver the sufficient momentum to lower atmospheric levels and electrons of this mixed beam can also account for the increase of Hα line emission in this location. The Hα line profile observed in kernel 2 has a lower intensity of the blue wing than in kernel 1, while its area is close to that of kernel 1. This indicates that the blue wing in kernel 2 is located further from the line core than in kernel 1 and the redshift in kernel 2 is larger than in kernel 1, for example, meaning that the mixed beam in kernel 2 should have a higher initial flux than in kernel 1. Hence, we suggest that the initial energy flux of the beam in kernel 1 can range from $(7 - 9) \cdot 10^{12}$ $erg \cdot cm^{-2} s^{-1}$.

For flaring event 2 and from a comparison of the blue wing intensities and shapes observed from Hα kernels 2 and 3, it is possible to suggest that the beam with similar parameters as in Hα kernel 2 could be injected into the atmosphere produced at 12:06:40 UT in Hα kernel 3 in footpoint F5 of the blue rope, which was 10 minutes later than Hα kernel 2 in seismic source 2. RHESSI started its observation at 12:08 UT, so we can only use the electron parameters derived from RHESSI for general guidance, assuming sympathetic flares occur in succession in

the same magnetic configurations, but not for a direct derivation of the energetic particle parameters.

Based on the observations of strong hard X-ray emission in FE1 and assuming the similar input in FE2, which is based on the similarity of Hα line blue wings in kernels 2 and 3, we assume that flare emission in both of the flaring events was produced by the injection of sub-relativistic mixed beams with power-law energy distributions and initial energy fluxes of $(8-12)\cdot 10^{12}\ erg\cdot cm^{-2}s^{-1}$ and a spectral index of 4. These beams are assumed to produce heating of flaring atmospheres in Coulomb collisions (Brown 1971; Syrovatskii & Shmeleva 1972). The beam parameters can be further tuned by the fit to the Hα line profile observed in kernels 1- 3, which is discussed in Section 3.

2.3. Hydrodynamic response of flaring atmospheres

For the physical conditions of flaring atmospheres, we use the models of hydrodynamic responses of the ambient plasma to short pulses of energy deposition by very intense energetic electron or mixed beams precipitating from the corona to the lower atmosphere (hydrodynamic model of type 1 discussed in the Introduction) (Somov et al. 1981; Zharkova & Zharkov 2007). The hydrodynamic model considers two energy equations (for electron and ion components), momentum and continuity equations, to describe the ambient plasma response to heating by beam electrons (Somov et al. 1981; Zharkova & Zharkov 2007) using a Lagrangian coordinate ξ. Plasma heating is caused by particle beams (Syrovatskii & Shmeleva 1972; Gordovskyy et al. 2005) and plasma cooling is caused by viscosity, or the motion between electrons and ions (Somov et al. 1981; Zharkova & Zharkov 2007). We consider the radiative energy losses in the corona (Cox & Tucker 1969) and by hydrogen emission in the chromosphere (Zharkova & Kobylinskii 1993; Kobylinskii & Zharkova 1996).

These models have the initial conditions of a quiet Sun chromosphere starting from a column depth just below the quiet Sun's transition region ($\xi = 10^{17}$ cm^{-2}) down to the beginning of the upper photosphere ($\xi = 10^{22}$ cm^{-2}). Details regarding these initial conditions are given in Somov et al. (1981), and they include (a) a constant temperature of 6,700K derived from semi-empirical calculations shown by a straight line in Fig. 2a, (b) hydrostatic equilibrium $v(0,\xi) = 0$, and (c) a density distribution is defined by the straight line in the logarithmic plot of Fig.2b. The numeric method for calculating the hydrodynamic response in a flaring atmosphere to the injection of power-law beam electrons is described in detail in the previous papers (Somov et al. 1981; Zharkova & Zharkov 2007).

The duration of beam injection was chosen to be 10 s, the initial energy flux of a beam varies as a triangular function in time, with a maximum of between 5 s and 6 s (Zharkova & Zharkov 2007). After solving the system of four partial differential equations with the initial and boundary conditions for a precipitating electron beam with given parameters (initial energy flux F_0 and spectral index γ), we obtain time-dependent distributions of electron T_e and ion T_i temperatures, ambient plasma density T, and macrovelocities v.

The heating of the QS chromosphere by a short pulse of a very intense beam of electrons or protons, or mix of them (type 1 model) (Somov et al. 1981; Duijveman et al. 1983; Zharkova & Zharkov 2007; Druett & Zharkova 2018), is shown to sweep the ambient plasma to the lower atmosphere, forming a new flaring atmosphere with a new corona, transition region, and chromosphere. This sweeping is followed by the plasma evaporation back to the corona combined with the formation of low-temperature condensation in the chromosphere moving as a shock to the photosphere. Hydrodynamic heating in the two other types of models (preheated and isotropic) would result in mild chromospheric plasma evaporation without sweeping, combined with the less intense shock moving downwards to the lower atmosphere with much smaller velocities and depths above the surface where these shocks occur instead reaching the solar interior (Polito et al. 2016; Fisher et al. 1985c,b; Allred et al. 2005; Kennedy et al. 2015; Bradshaw & Cargill 2006), which are not relevant for the atmospheres associated with sunquakes.

2.4. Simulation of hydrodynamic responses

Hydrodynamic responses of flaring atmosphere caused by 10-second pulses of intense particle beams (either mixed or pure electrons) are shown to lead to quick sweeping of QS chromosphere plasma towards the photosphere and beneath, forming hydrodynamic shocks, which are shown to first move with large velocities towards the solar interior and to later return to the pre-flare conditions. The phases of this process include the initial heating by beam particles in Coulomb collisions lasting 10 seconds after the beam onset, which produces a hydrodynamic response of the ambient plasma to this heating followed by the slow cooling off of the ambient plasma and its return to the pre-flaring position and conditions. Hydrodynamic responses start to develop over a minute after the beam onset and last up to an hour because of a larger characteristic hydrodynamic time (order of 30 seconds) caused by thermal diffusion (Shmeleva & Syrovatskii 1973).

Hence, the hydrodynamic simulations for the flaring atmospheres heated by a mixed beam in the footpoints associated with the seismic sources 2 and 3 are plotted in Fig.2 (left column). We also ran the other hydrodynamic simulations with lower initial energy fluxes of $10^{11}\ erg\cdot cm^{-2}s^{-1}$ and $10^{10}\ erg\cdot cm^{-2}s^{-1}$ (see the plots in Druett & Zharkova 2018, not shown here) reduced by a few orders of the magnitude down from the initial energy flux of $10^{13}\ erg\cdot cm^{-2}s^{-1}$ used for this flare and shown a comparison of the simulated and observed Hα line emission for all three hydrodynamic models. For a comparison of the current conditions for sunquake 2 in 6 September 2017 flare with the conditions of the sunquake formation in the flare of 6 September 2011, in Fig. 2 (right column) we present the hydrodynamic models simulated for the injection of an electron beam with the initial energy flux of $4.3\cdot 10^{11}\ erg\cdot cm^{-2}s^{-1}$ and spectral index of 4 (Macrae et al. 2018). These two hydrodynamic models can provide important insight into the mechanisms of formation of the acoustic signatures in two flares discussed in Section 4.2.2.

It can be noted that the hydrodynamic responses induced by a mixed beam (Fig.2, left column) in the flare from 2017 and by the electron beam (Fig.2, right column) in the flare from 2011 are very different despite the fact that they both show a quick increase in the kinetic temperatures within the first 5 seconds after the beam onset. However, compared to the initial chromospheric temperature of 6700K, the mixed beam causes a much stronger increase of the kinetic electron temperature in the corona up to 40 million Kelvin (MK) (Fig.2a), while the kinetic temperature growth caused by a less intense beam increases only to 10 MK. The ambient plasma density in the atmosphere heated by either beams (Fig. 2b) is significantly reduced in the flaring corona from the initial QS chromospheric magnitude (10^{10} cm^{-3}) to $10^9 - 10^8$ cm^{-3}, to form the new corona of a flaring atmosphere (Somov et al. 1981). As expected, during the time of the beam injection (10s), there is also a larger reduction of the coronal density because a larger amount of plasma was swept by a precipitating mixed beam compared to the electron one (see Fig. 2b). These trends are similar to the hydrodynamic models that are heated by electron beams with the same parameters reported by Fisher et al. (1985c,b).

This stronger plasma sweeping in the flaring atmosphere by the mixed beam leads to a faster speed of chromospheric plasma evaporation back to the corona that approaches 1600 km/s compared to 1300 km/s for an electron beam as shown in Fig. 2c (compare the left and right plots). Furthermore, the fast dynamics of the coronal plasma heating by a mixed beam leads to very strong, explosive evaporation (with velocities above 1500 km/s) of the chromospheric plasma to the coronal levels up to 8000 km above the surface, while the electron beam would cause much milder evaporation to the heights of about 1500 km above the surface approaching the macrovelocities just above 1200 km/s.

The upward motion of the flaring plasma is reflected in the macrovelocity plots (Fig. 2c), showing negative (upward) macrovelocities that correspond to the evaporation of chromospheric plasma to the newly formed corona at the column depths between 10^{17} and 10^{19} cm^{-2}. This evaporation lasts for 1000-2000 seconds even after the beam stops expanding with the increasing velocities upwards to the QS corona (Somov et al. 1981; Fisher et al. 1985c,b; Zharkova & Zharkov 2007). The evaporation velocities range from a few tens of km·s^{-1} (at 1s) up to 1500 km·s^{-1} (at 30−100 s). As shown earlier (see section IV and Fig. 5 in Fisher et al. 1985b), these high upflow velocities naturally appear in the gasbag models (Somov et al. 1981; Fisher et al. 1985b; Zharkova & Zharkov 2007). These higher velocities of evaporation are larger than those measured in the EUV observations of the older missions (Doschek et al. 1979; Antonucci et al. 1982; Zarro et al. 1988) as well as by the modern instruments, such as EIS/Hinode, the Atmospheric Imaging Assembly (AIA/SDO) (Lemen et al. 2011), or the EUV variability Experiment (EVE/SDO) (Woods et al. 2006; Doschek et al. 2014; Milligan et al. 2014; Milligan 2015).

However, the lack of observations with high upflow velocities above 1000 km/s can occur for a few reasons: a) the dynamic range of the CCD sensors whose extra-exposure time during a flare onset, if not reduced, can lead to the over-exposed emission in hot coronal lines, where such large upflow velocities are expected to occur; b) the coronal density at the upper heights where these velocities occur becomes too low, as shown by hydrodynamic simulations (Fig.2b), so the abundances of hot ions with a large upward motion on the line of sight are not sufficient to produce a notable emission, so that the emission measures are too weak, and c) the lines selected by the EUV instruments can only observe lower temperature plasma that formed at the lower corona where the macrovelocitis are restricted up to 400 km·s^{-1} (Doschek et al. 2014; Milligan 2015).

While the theoretical hydrodynamic temperature and macrovelocity curves show a strong increase in the temperature up to 40 MK and macrovelocities exceeding 1400 km/s, these cannot be observed by the modern instruments with restricted dynamic ranges of physical parameters aimed at the hot plasma of lower solar corona and the transition region, or because of lower densities of the flaring corona plasma after it was swept by very powerful particle beams. Evidently, after the beams are switched off, the plasma cooling in the upper atmosphere that is heated by mixed beams (left column) is much slower than in the atmosphere that is heated by the electron beam (Fig. 2, compare left and right columns). Thus it would be beneficial to observe the emission in these hot coronal levels in very hot lines, allowing one to catch large plasma upflows with the future instruments for SXR observations of hot coronal plasma with wider energy ranges.

Besides large upflows, the abrupt energy deposition by super-energetic particle beams within a short timescale of 10 seconds leads to a formation in the flaring chromosphere of low temperature condensations, which move downwards to the photosphere and interior with supersonic velocities as shocks, thus producing large downflows (Somov et al. 1981; Zharkova & Zharkov 2007; Zharkova & Zharkov 2015). By comparing the panels in Fig.3 for different times after the beam injection, it is evident that the higher the initial energy flux the larger the speed of a shock produced by hydrodynamic response. For example, for the mixed beam, the shock velocities of $50 - 100$ km·s^{-1} are reached just 1 second after the beam onset (see Figs. 2c and 3a), while after 5 seconds these velocities sharply increase to $200 - 250$ km·s^{-1} for a weaker beam (see Figs. 2c, right plot and 3a) and 380-400 km/s for a more intense beam (see Figs. 2c, left plot and 3b. The plasma of the shocks has slightly (up to 10^4 K) increased temperatures and much larger densities (a factor of 10^{13} cm^{-3} up to 10^{14} cm^{-3}) for the most powerful mixed beam (Fig. 2b, left plot).

Hence, these shocks have large densities and high macrovelocities that are capable of delivering very large momenta to the lower atmosphere and solar interior. It is important to determine how deeply these shocks can travel into the QS solar atmosphere. For a comparison, in order to clarify this point, in Fig. 4, we present the relationship between the linear depth of the quiet Sun (axis Y) versus the column depth of a flaring atmosphere (axis X) for the beams with the initial fluxes of 10^{12} $erg/cm^2/s$ (a) and 10^{11} $erg/cm^2/s$ (b). It is evident that the weaker beam in Fig. 4b sweeps the ambient plasma downwards to a column depth of 1-2 units of 10^{19} cm^{-2} or a particle density of about 10^{13} cm^{-2} that is just close to the quiet Sun surface if compared with the linear depth, which is shown in

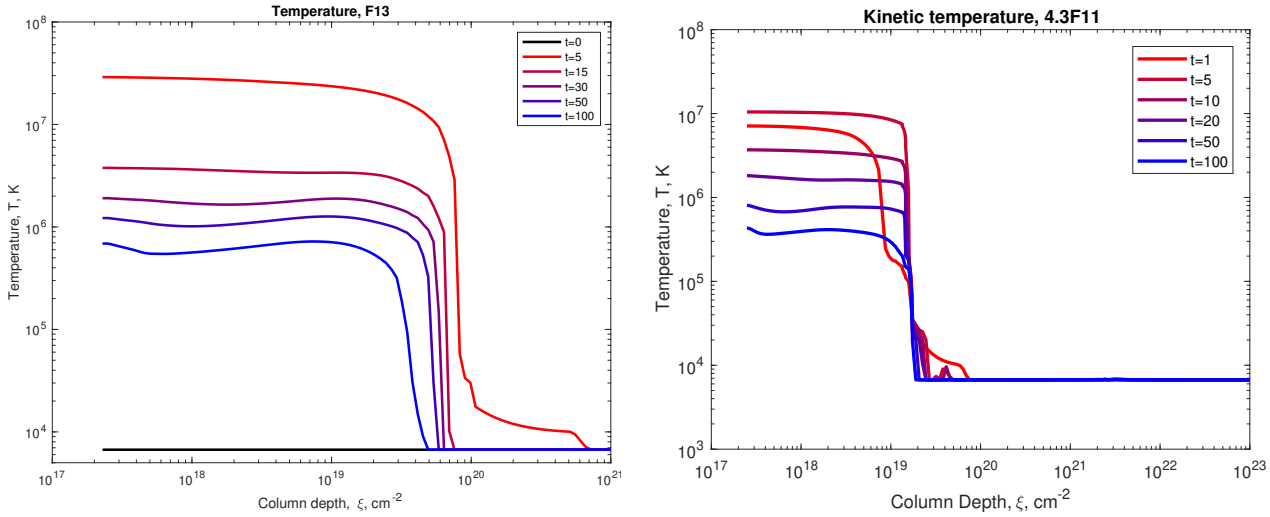

(a) Electron temperature

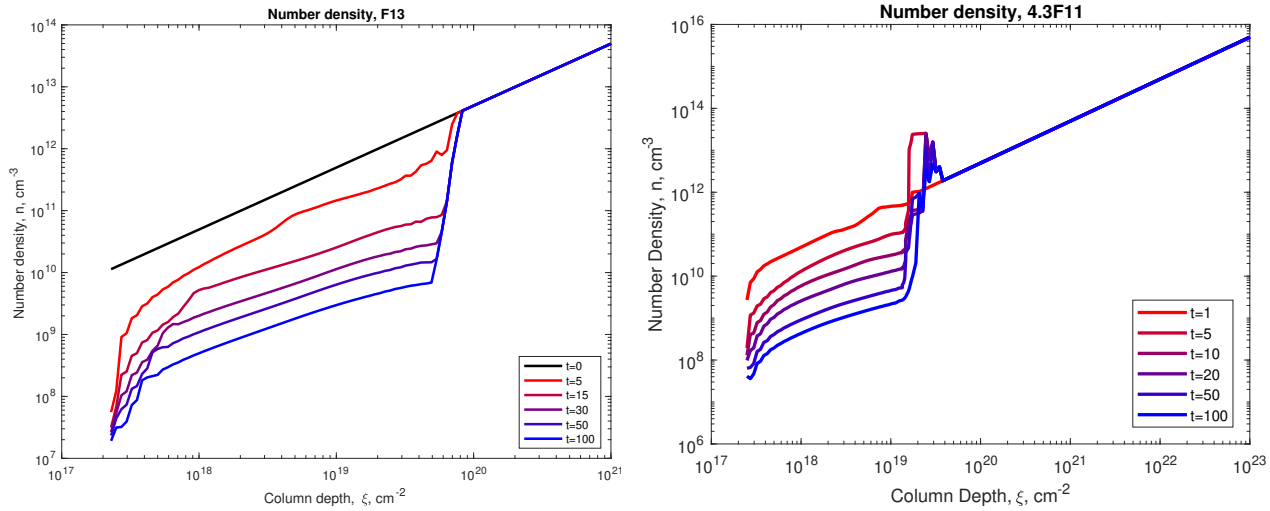

(b) Ambient density

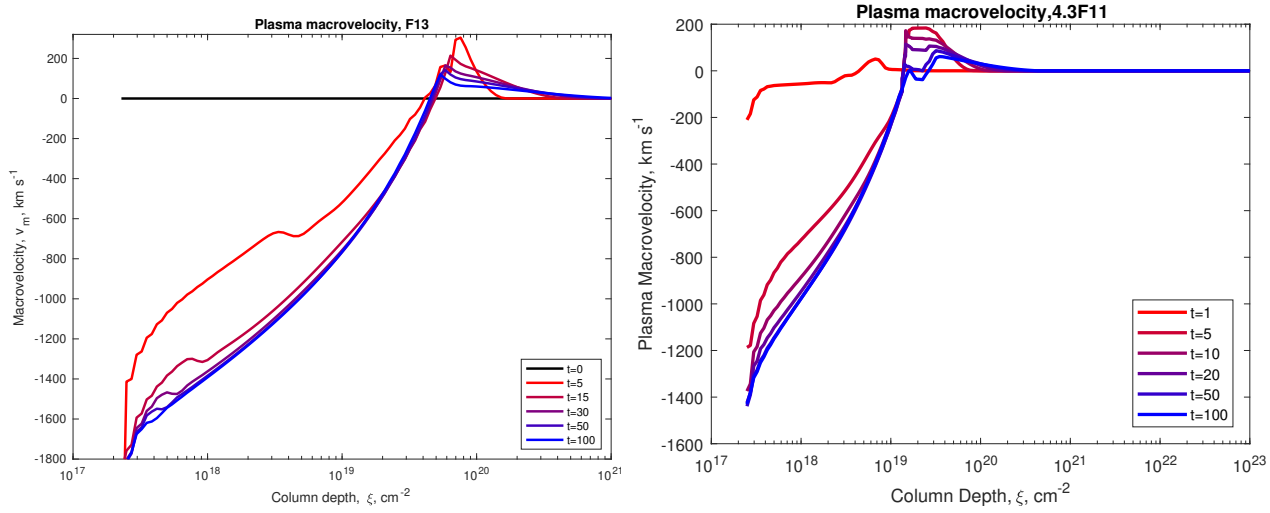

(c) Macrovelocity

Fig. 2. Column depth dependencies of electron kinetic temperature, K (top row), ambient plasma densities, cm^{-3} (middle row), and plasma macrovelocities, $km \cdot s^{-1}$ (bottom row) simulated as hydrodynamic responses to the injection of power-law particle beams with the initial energy flux of 1.0×10^{13} $erg \cdot cm^{-2} \cdot s^{-1}$ and the spectral index of 4 (left column) and with the initial energy flux of 4.3×10^{11} $erg \cdot cm^{-2} \cdot s^{-1}$ and the spectral index of 3.5 (right column).

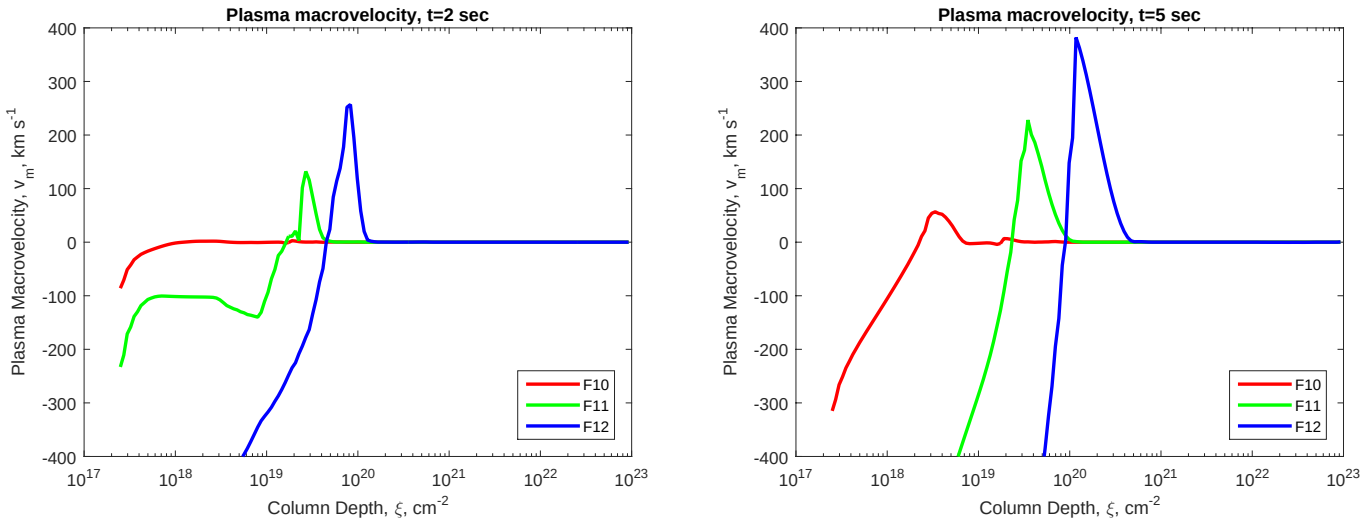

(a) Shocks at 2 s for different fluxes

(b) Shocks at 5 s for different fluxes

Fig. 3. Left panel: Close-up look at the macrovelocities of the shocks produced by electron beams in the first 2 s (a) and 5 s (b) after the beam onset for different initial energy fluxes and the same spectral index of 3.

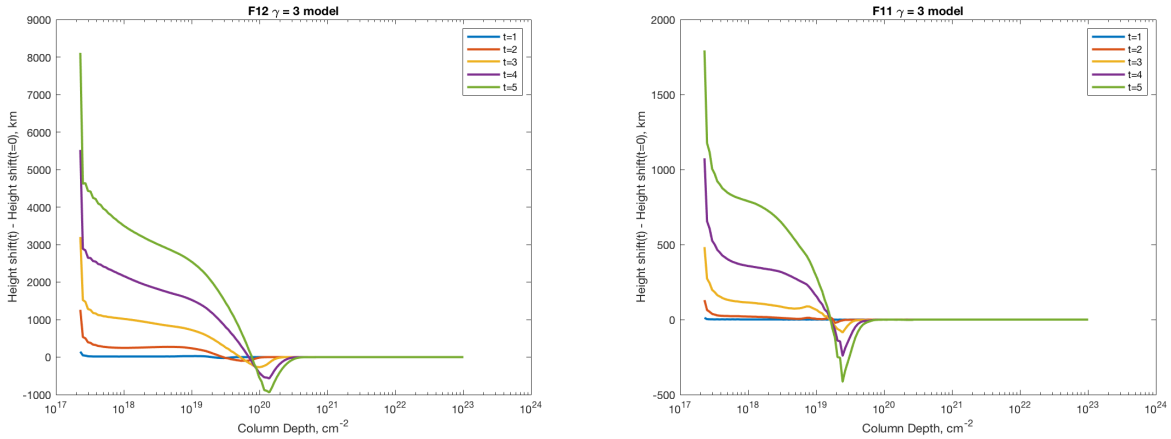

(a) Linear depths for F12 model

(b) Linear depth for F11 model

Fig. 4. Linear depths (Y-axis) versus column depths (X-axis) of hydrodynamic responses of a flaring atmosphere to the injection of a beam with the initial flux of f 1.0×10^{13} erg·cm^{-2}·s^{-1} (left) 1.0×10^{11} erg·cm^{-2}·s^{-1} (right) and a spectral index of 3.0. Note that the zero point in axis Y indicates the position of the quiet Sun photosphere.

Fig. 4. While the stronger beam shown in Fig. 4a has much greater power, it thus sweeps the ambient flaring plasma down to the column depth of 10^{20} cm^{-2} with a density of a factor of 10^{13} cm^{-2} that is below the QS solar surface, appearing in the solar interior. Hence, both shocks move with a supersonic speed into the deep solar interior.

Therefore, the shock produced by a more intense beam (Fig.4a) starts its motion deeper in the interior than the shock driven by the weaker beam (Fig. 4b), and it has a larger density. Thus, the larger shock delivers larger momentum while moving from the deeper interior depth. This means that the weaker beam forms a shock just beneath the photosphere and this shock travels with a supersonic speed in the solar interior at a distance of <1000 km when it travels with the speed higher than the local sound speed (Zharkova & Zharkov 2007; Macrae et al. 2018). In contrast, the more intense beam, which sweeps the ambient plasma much deeper into the solar interior, forms the shock inside the solar interior at a closer depth to the solar surface and it travels with a supersonic speed for the larger distance >1000-1500 km in the solar interior (Zharkova & Zharkov 2015). These differences in the depth of deposition, velocity, and density of the shocks affect the conditions for formation of acoustic waves in the solar interior. The investigation of the shocks derived for the physical conditions in the 6 September 2011 and 2017 flares is presented in Section 4.

2.5. Probing hydrodynamic results with the EIS observations

The HD models that are heated by the mixed beam produce, within 5-15 seconds, very fast heating of a flaring atmosphere above 40 MK, which may explain an early brightening of flaring atmosphere in 1700 Å leading to its over-exposure of this AIA emission. For the HD model that is caused by the powerful mixed beam, the EUV emission can be observed by the EIS instrument in He II and Fe XXIII emission at the very beginning of the flare onset if the flaring atmosphere temperature approaches the temperature range suitable for the radiation temperatures of these transitions: 7-20 million K for Fe XXIII and about 10^5 K for the He II line. It can be seen that the temperature magnitudes that are favourable for this Fe XXIII emission appear immediately during the beam onset and continue to exist after the beam offset, while at 15-30 seconds from the beginning of the event, the atmosphere cools to a few million K shown by the dark red and purple lines in Fig. 2a. The emission of the He II line is expected to appear in this model a bit (30-50 seconds) after the beam offset. At the time of 50 seconds, the hydrodynamic shock velocity is also reduced if it is heated by a mixed beam (see Fig.2c, left plot) or if this shock starts returning to the pre-flare atmospheric level if it is heated by an electron beam (compare the left and right plots of Fig.2c).

The explosive evaporation of the plasma heated by a mixed beam starts from the very first seconds of observations with high macrovelocities of 100 km·s^{-1} (see Paper 1 Zharkov et al. 2020), similar to the macrovelocities simulated in the lower flaring corona (Fig.2c, left column) for a mixed beam, and approaching the velocities of 400-500 km·s^{-1} only 5 seconds after the beam onset. Later these macrovelocities are reduced to 250 km/s at 30-50 s after the event onset when these magnitudes are observed by the Fe XXIII line (shown in Figs. 10-12 in paper 1). As shown in paper 1, the spectrograms for the Fe XXIII 263.76 Å line for event 1 occurring in the FP3 of seismic source 1 reveals the large blueshifted velocities of the upflows of 400 kms^{-1}, which are similar to the simulated velocities for heating by a mixed beam (blue line in Fig. 2c, left plot). Moreover, for SQ2 the blueshifts in the line of Fe XXIII 263.76 Å show the macrovelocity of explosive evaporation, exceeding 400 km/s much faster than in the atmosphere with SQ1, which indicates a stronger shock occurring in the location of SQ2. This, in turn, led to the observation of secondary ripples, or the additional ridge in the time-distance diagram, constituting a double bounce of acoustic waves in the interior beneath the flare.

This is combined with the downflows of > 100-200 kms^{-1} seen in the He II spectrograms associated with SQ1 and SQ2. The EIS observations in He II 256 Å in SQ1 and SQ2 locations appear 30 s after the onset of FE1 confirming that the starting time of SQ1 and SQ2 is 20-25 s earlier than the redshift in the He II line. This redshift exists for about a minute, as is shown in the bottom first three plots in Figs. 9 and the three plots from the right in Fig.10 in Paper 1. It can be noted that this He II line first captures the downflows, which after a minute or so are followed by upflows when the swept plasma starts returning to the pre-flare positions with the magnitudes of macrovelocities that are close to those predicted by the hydrodynamic (HD) simulations for the heating by a mixed beam (in SQ1 and SQ2) shown in Fig. 2 (left column). It can be seen that the blue line shifts show the upward macrovelocities in Fig. 2c, which approach 400 km/s.This is similar to what was measured in Paper 1 by the EIS instrument for the location of seismic source 1. At the same time, the downward motion that was modelled for this event also reaches the macrovelocity of 150-200 km/s (purple line in Fig. 2).

However, the He II 256 Å spectrograms with a Doppler velocity taken in the location of a largest sunquake described in Paper 1 reveal that, similar to the simulations shown in the left plot of Fig. 2c, the redshifts appear 15-20 seconds after the plasma started cooling off to the temperature when the He II emission becomes observable and their velocities approach several hundred kms^{-1}. The simulated and measured blueshifts start from 150 km/s and approach 300 km/s within a short timescale of 15-30 seconds. The observed redshifts in an excess of 250 kms^{-1} are well-correlated with the appearance of the largest sunquake 2 and the redshift in the Hα kernel 2 in footpoint FP4, which is associated with the green magnetic rope (see Fig. 1).

Also in flaring event 2, the EIS in He II 254 Å observed both blueshifts up to 200 kms^{-1} as reported in Paper 1, while the redshifts in excess of 150 kms^{-1} are well-correlated with the possible sunquake 5 and Hα kernel 3, which seem to have a similar heating and seismic response as in seismic source 2. These observations can still be explained by the hydrodynamic simulations of the atmosphere heated by the powerful mixed beam, as shown in Fig. 2 (left column).

3. Radiative response of hydrogen atoms

3.1. Description of radiative model

Based on the hydrodynamic models calculated above, our other papers (Druett et al. 2017; Druett & Zharkova 2018, 2019), and in taking into account that the characteristic hydrodynamic time (30 s) (Shmeleva & Syrovatskii 1973; Somov et al. 1981) is much longer than the characteristic radiative time (a fraction of a second) (Shmeleva & Syrovatskii 1973), one can apply the radiative models for hydrogen emission to the hydrodynamic models calculated for each second. The hydrogen emission in a flaring atmosphere was calculated using the second part of the HYDRO2GEN code utilising a full non-LTE approach for a five level plus continuum hydrogen model atom considering radiative transfer in the Lyman series, Lyman continuum, as well as in Balmer and Paschen ones (Druett et al. 2017; Druett & Zharkova 2018, 2019).

We consider the hydrogen atom excitation and ionisation by thermal and beam electrons as well by external and diffusive radiation (radiative transfer). The radiative transfer and statistical equilibrium equations were solved numerically by iterations defining the source functions in each atomic transition and ionisation degree of hydrogen atoms (Druett & Zharkova 2018) in the atmosphere at any given instant during the hydrodynamic response. The solutions of the radiative transfer equations were found using the L2 approximation introduced

by Ivanov & Serbin (1984). The simulated Hα line intensities were calculated from the source functions derived for atomic transitions between levels 3 and 2 using Voigt's absorption profiles (Druett & Zharkova 2018).

For non-thermal hydrogen excitation and ionisation rates by beam electrons, the analytical formulae derived by Zharkova & Kobylinskii (1993) were used. The authors showed that non-thermal collisional excitation and ionisation rates of hydrogen dominate above the thermal ones in flaring atmospheres from the chromospheric depths just below the transition regions (see Fig. 3 in Zharkova & Kobylinskii 1993). The stimulated photo-excitation by external radiation, de-excitation, and ionisation rates by thermal electrons for given physical conditions in flaring atmospheres were also taken from Zharkova & Kobylinskii (1993).

3.2. Simulated Hα line profiles and their fits to observations

In the X9.3-class flare on 6 September 2017 for flaring event 1, we managed to detect a noticeable increase of Hα line emission in the two Hα kernels 1 and 2, and for the flaring event 2 in Hα kernel 3. However, the extracted emission line profiles in kernels 1-3 were rather unusual as the emission increased with the wavelengths over 3 Å (spectral window of the CRISP instrument) as reported in Paper 1 (Zharkov et al. 2020). The Hα-line profile derived in kernel 1, coinciding with seismic source 1, is located in footpoint F3 at the northern end of the green magnetic rope (see Fig. 1a). We note that Hα-line kernel 2 was co-temporal with seismic source 2 and it is located in footpoint F4 at the southern end of the green magnetic rope in Fig. 1a. No Hα-line kernels were detected in the location of seismic source 3, which has the most peculiar dynamics that will be described in a forthcoming paper. The Hα line emission in kernel 3 occurred in the location that is close to that of seismic source 2, but during flaring event 2 about 10 min later than in kernels 1 and 2. We assumed that in kernel 3 there should also be a seismic source 5, which occurred in the location close to F4 during FE2.

In general, the hydrodynamic radiative simulations of hydrogen emission show that during the flare and at the very first few seconds after the beam onset, Hα becomes an emission line revealing a strong increase in the central and wing emission caused by enhanced ionisation and excitation induced by energetic power-law electron beams (Druett et al. 2017; Druett & Zharkova 2018). Furthermore, in the very first seconds, Hα line profiles become strongly redshifted, as is shown in Fig. 5. These line profiles, calculated for different particle beam parameters, were similar to what has been observed in the past in the other flaring events with spectral windows of ±8 Å (Ichimoto & Kurokawa 1984; Wuelser & Marti 1989).

By looking at the observed Hα-line profiles reported in paper 1 (Zharkov et al. 2020), we recognised that in kernels 2 and 3, the profiles are clear blue wings; there is a far wing in kernel 2 and a near wing in kernel 3. In kernel 1, the observed Hα line profile can be considered at first to be the regular profile with self-absorption and to be a strongly increased red horn in the line core reported previously for near stationary and slightly moving atmospheres (Ding & Fang 1996; Kuridze et al. 2015; Druett et al. 2017). However, it turns out that this is not the case because of the very strong intensity of the whole emission and, particularly, due to the red wing of the profile, which is higher than the Hα line profiles even in the cores simulated for weaker beams. Furthermore, the observed Hα line intensity in kernel 1 still increases as it reaches the edge of the available wavelength window (+1.5Å). However, based on the features present in the observation profile, it is certainly likely that we observed the near blue wing of the line since the line may not be so greatly redshifted as in kernels 2 and 3.

For these reasons, we calculated the Hα-line profiles produced from hydrogen atoms by combined thermal and non-thermal excitation and ionisation by beam electrons in flaring atmospheres that are heated by: 1) a mixed beam with the initial energy flux of 1.0×10^{13} erg·cm^{-2}·s^{-1} (model F13), the spectral index of 4 as derived for flaring events 1 and 2 in Paper 1 (Zharkov et al. 2020), and 2) electron beams with much smaller initial energy fluxes of 1.0×10^{11} erg·cm^{-2}·s^{-1} (model F11) and 1.0×10^{10} erg·cm^{-2}·s^{-1} (model F10) for the spectral index of 4, in case the electron component in the mixed beam in kernel 1 was somewhat smaller than in kernels 2 and 3. Interestingly, none of the simulated Hα line profiles show self-absorption in the line cores unlike what has been reported earlier in weaker flares (Kuridze et al. 2015; Druett et al. 2017). These unusual Hα line profiles emitted in the atmospheres affected by stronger beams are likely to be defined by stronger non-thermal ionisation of hydrogen atoms. This, in turn, reduces the number of neutral hydrogen and, thus, the optical thickness in Hα lines, which makes the line profiles without self-absorption.

It can be seen that the simulated Hα line profiles for any HD model, as shown in Fig. 5, are mainly dominated by the downward motion of the hydrodynamic shocks shown in Fig. 3, which are generated in response to the injection of beam electrons with different fluxes or to the injection of mixed beams with electrons (shown in Fig. 2c). Depending on the shock velocity, which varies from 40 to 380 km/s, the redshifts in Hα-line profiles can vary from 1-2 Å (5a), 3-4 Å (5b), or to >5 Å (5c and 5d), which were often observed with spectral windows of ±8 Å in other flaring events (Ichimoto & Kurokawa 1984; Wuelser & Marti 1989).

The Hα line profiles simulated for the green rope footpoints in kernels 1 and 2 for flaring event 1 are based on the hydrodynamic models simulated for a mixed power-law particle beam F13 (see Fig. 2, left column) in the flaring atmosphere associated with seismic source 1 (footpoint FP3 in the northern end of the green rope in Fig.1) and with seismic source 2 (footpoint FP4 in the southern end of the green rope), as concluded in Paper 1. Since this KONUS observation does not have a spatial resolution, we can only rely on the observed kernels of Hα emission and seismic signatures in the kernel locations for an evaluation of the parameters of particle beams producing their emission co-temporally with HXR emission (see sections 2.2 and 2.4). The total energy flux of the high energy emission observed by KONUS in the areas of Hα kernels 1 and 2 was between $(8 - 12) \cdot 10^{12}\ erg/cm^2/s$ (or model F13), as derived in Paper 1.

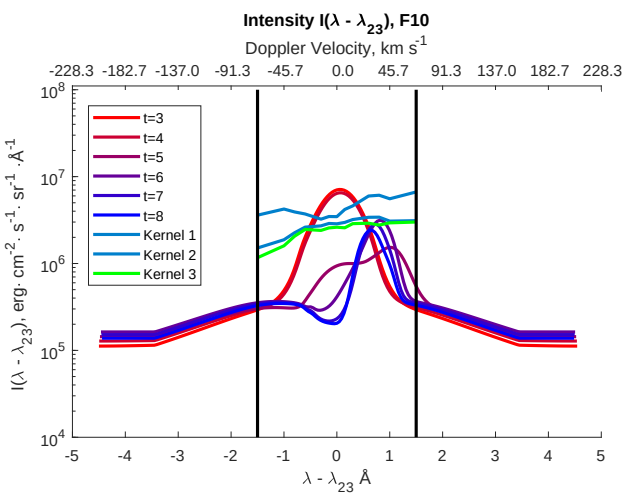

(a) Hα kernels vs F10 model

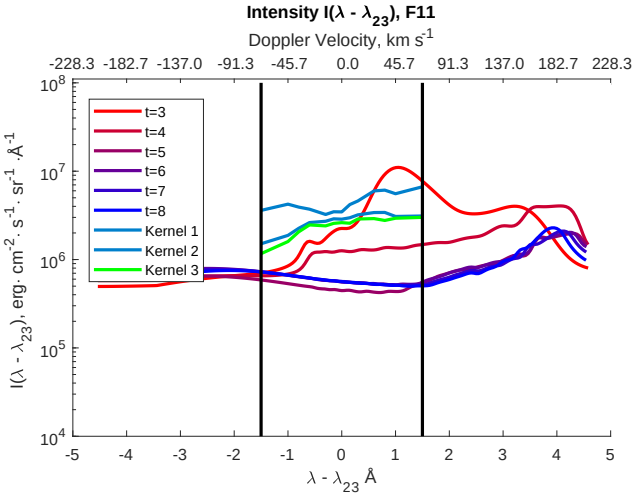

(b) Hα kernels vs F11 model

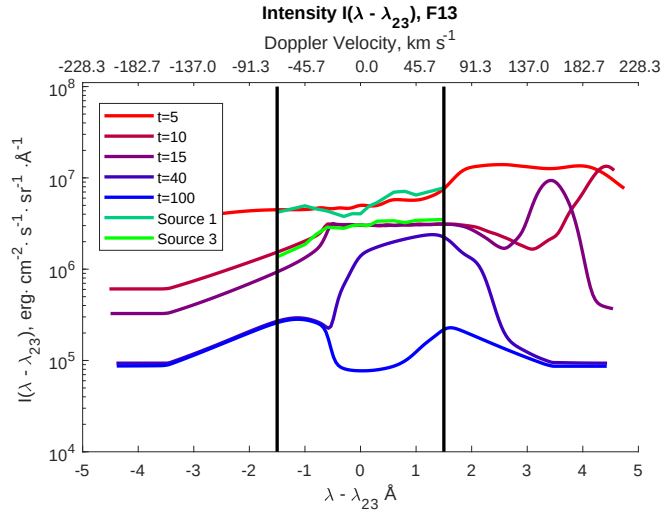

(c) *Hα* kernels 2 and 3 vs F13 model

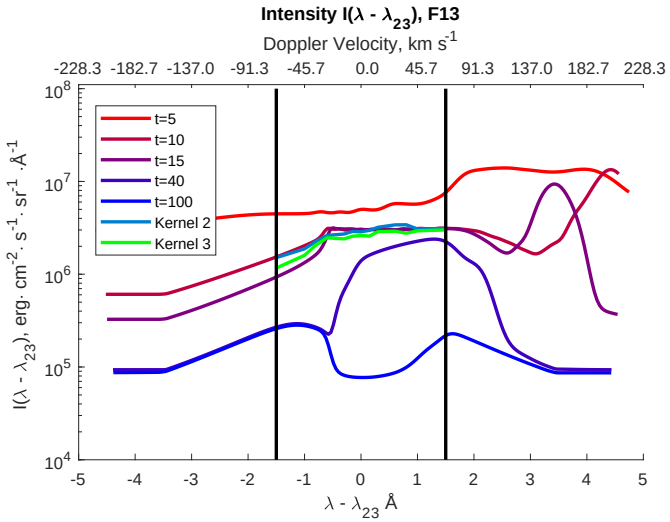

(d) *Hα* kernels 1 and 3 vs F13 model

Fig. 5. Observed Hα-line profiles in kernels 1-3 overplotted on the Hα line profiles simulated with the HYDRO2GEN code (Druett & Zharkova 2018) in flaring atmospheres produced by the following. (a) An electron beam with a spectral index of 4 and an initial energy flux of 10^{10} $erg \cdot cm^{-2} s^{-1}$. (b) An electron beam with a spectral index of 4 and an initial energy flux of 10^{11} $erg \cdot cm^{-2} s^{-1}$. (c) A mixed beam with a spectral index of 4 and an initial energy flux of 10^{13} $erg \cdot cm^{-2} s^{-1}$. d) A mixed beam with the same parameters as in c). The observed Hα line profiles are shown in kernel 1 (blue line), kernel 2 (light blue line), and kernel 3 (green line). The vertical lines show the spectral window ±1.5 Å for the CRISP/SST Hα line observations.

Since these estimations for the initial energy fluxes of the beams in flaring atmospheres from the areas of Hα kernels were not derived directly from the HXR observations, located in the kernels as well, but on some assumptions about how the total beam energy was redistributed between a few footpoints where the SQs and Hα kernels occurred, one can only estimate the order of magnitude of the initial energy flux of particle beams. While the exact coefficients in front of the order of magnitude of the initial energy fluxes can be flexible because they are somehow dependent on the assumptions. Therefore, we simplified the interpretation by only considering the basic initial energy flux F13, and we discuss possible deviations of the simulated profiles from the observed ones, in particular for kernels.

The Hα-line profiles derived at kernels 1-3 are plotted in different colours on the top of model simulations of these profiles, which were calculated for the atmosphere that is heated by beams with the initial energy fluxes relevant to models F10, F11, and F13, as shown in Fig. 5. It can be seen that the observed blue wings of Hα line profiles in all three Hα kernels only fit model F13 at the times of 5 s (kernel 1) and 15 seconds (kernels 2 and 3), while the observed Hα blue wing intensities were much higher than those simulated for the HD models that were heated by the beams with lower energy fluxes (F10 or F11). The vertical lines show the spectral window of CRISP/SST, which demonstrates the limits of the observations of Hα line profiles with the largely redshifted cores.

Let us keep in mind that Hα-kernel 2, which occurred at 11:55:50 UT during flaring event 1, is associated with seismic source 2. The redshift in the simulated Hα line profile of kernel 2 in the hydrodynamic model of a flaring atmosphere, heated by a strong mixed beam, reaches a maximum of about 5-6 Å at 5 s, or just after the beam offset, when the downward velocity of 380 km·s^{-1} is maximal, while dropping below 300 km/s after 15 seconds (see Fig. 2c, right plot or Fig. 3a). Hence, the simulated Hα line profile in kernel 2 is found to be strongly redshifted by more than 5.0 Å from the central wavelength (λ = 6563 Å), corresponding to an averaged Doppler velocity of 268 $km \cdot s^{-1}$. The core of this Hα line profile cannot be observed by CRISP because it is strongly redshifted far outside the CRISP spectral window of ±1.5 Å.

As a result, we infer that the observed Hα-line profiles in the spectral window of ±1.5 Å only show far blue wings in the Hα line because the line is strongly redshifted by the shock induced by a mixed beam with the high initial energy flux. Hence, the observed Hα-line profiles in kernel 2 are close to the simulations made for the F13 model about 15 seconds after the beam onset, as shown in Fig. 5d, with a much lower intensity in this blue wing. For a possible observation of Hα emission by CRISP in powerful flares, either a fast shift of the spectral window to the red wing of the line should be used or the observed Hα line profiles a minute or so after the flare onset should be used. While for Hα kernel 1, the blue wing fits the line profile better at 5 s after the beam onset, which might signal the timing when the beam in this flaring atmosphere reaches footpoint FP3 where this kernel was measured.

The Hα-kernel 3 was observed at 12:06:48 UT in flaring event 2, which occurred about 10 minutes after flaring event 1. The kernel 3 was located close to seismic source 2, so that the seismic signatures in this location should become overlapped with those issued in FE1. The observed Hα line profile fits the simulated Hα line profile rather well that was calculated for model F13 (see Fig. 5c). The second flaring event was only observed by Lyα and GOES emission and by Hα emission with the CRISP instrument having a high spatial resolution. We note that 1.2 minutes after this event, there were HXR observations by RHESSI payload with the HXR contours located exactly in the location of Hα kernel 3, which is shown in Paper 1. In the absence of HXR emission for this event, we can only speculate that the same magnetic configuration has produced a sympathetic flaring event after FE2, which has accelerated particles to power law beams with the close parameters as in FE2. By comparing the observed Hα line profile in kernel 3 with the simulated ones shown in Fig. 5, we deduce that the best fit is achieved if the flaring atmosphere in footpoint F4 was heated by a powerful mixed beam with an initial energy flux of about, or above, $(6-8) \cdot 10^{12}$ erg·$cm^{-2}s^{-1}$ (still of the same order of magnitude as in Hα kernels 1 and 2).

This shock in flaring event 2 should produce a noticeable seismic response in seismic source 5, which can be comparable with what was observed in seismic source 2 in flaring event 1 that occurred 10 minutes before the flaring event 2. However, this hypothetical seismic event 5 was obscured by the ripples from seismic events 2 and 3, thus, it cannot be detected by either methods of sunquake detection.

3.3. Simulated Paschen continuum (WL) emission

The temporal variations of white light emission at the WL locations in Hα line kernels 1 and 3, which were observed from WL images from the HMI/SDO instrument, can be also compared with the simulated temporal profiles in the Paschen continuum of hydrogen atoms that were obtained using non-LTE simulations. It is shown by (Druett & Zharkova 2018) that the Paschen continuum emission in flares originates in the chromosphere and photosphere, and the beam electrons are the main agents producing Paschen continuous emission, which is seen as white light emission. The contribution functions for Paschen continuum that are responsible for white light emission are presented in Paper 1, assuming that in WL kernel 1 (Hα kernel 1) the emission is produced by the beam with an initial energy flux of $(4-5) \times 10^{10}$ (F10) and WL kernel 2 (Hα kernel 3) the WL emission is produced by the beam with the energy flux of 10^{13} (F13).

This WL emission occurs because of the strong ionisation and excitation of non-thermal electrons, which enhance Paschen continuum contributions at all atmospheric levels (Druett & Zharkova 2018). It is important to note that, with the injection of powerful beam electrons and the non-thermal ionisation by them of hydrogen atoms, the Paschen continuous emission is found not only to be produced in the photosphere, as occurs in the QS, but mostly in the chromosphere, as is shown in the left plot of Fig. 6 for a moderate beam. The more powerful beam produces much stronger, in terms of the two orders of magnitude, Paschen continuum emission in both the photosphere and the chromosphere. Non-thermal ionisation of hydrogen atoms by beam electrons is, evidently, the key process producing the main contribution for white light flares (Druett et al. 2017; Druett & Zharkova 2018), in general, as well as for this particular event on 6 September 2017.

Now by looking at the contribution functions of Paschen continuum produced by beams F10 and F13, one can note that the intensity of this emission for the F13 beam is more than an order of magnitude higher than for model F10. This is governed by a large opacity of Lyman continuum emission in the F13 model (Druett & Zharkova 2019), which increases the intensity of all hydrogen continuum emission. In particular, Paschen continuum emission for the F13 beam is formed at deeper atmospheric levels and has a much longer existence compared to that induced by a less powerful beam from model F10. Since the observations confirm the very intense and long-lasting white light emission of the flare from 6 September 2017 combined with the fit of Hα line profiles in the kernels for FE1 and FE2, we can confirm that the optical emission in this flare was produced by a very intense beam.

The emission in the first WL kernel (Fig. 6c) is likely to be caused by a weak beam as derived from kernel 1 of Hα emission in Section 3.2, whose line profile is likely produced by the rather weak beam. Whereas, the second white light kernel 2 (Fig. 6d) was co-spatial to *Hα* kernel 3 in flaring event 2, which is associated with a much stronger electron beam that was injected after 12:06:40 UT. The electron beam in flaring event 2 produces stronger ionisation of the ambient hydrogen and stronger Lyman continuum, which controls the continuous

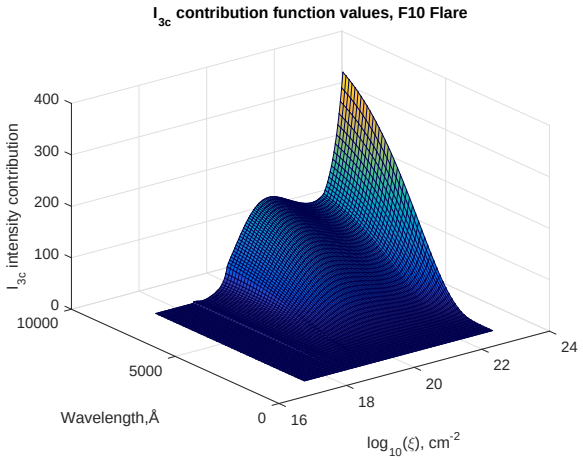

(a) Contribution function 1

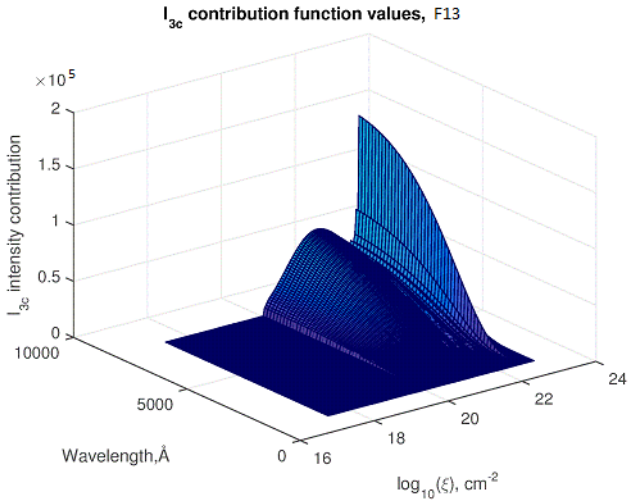

(b) Contribution function 2

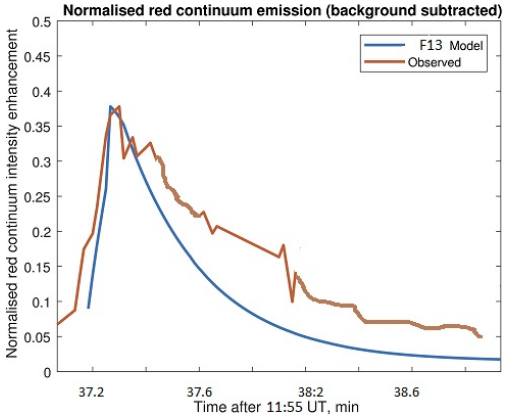

(c) Light curve 1

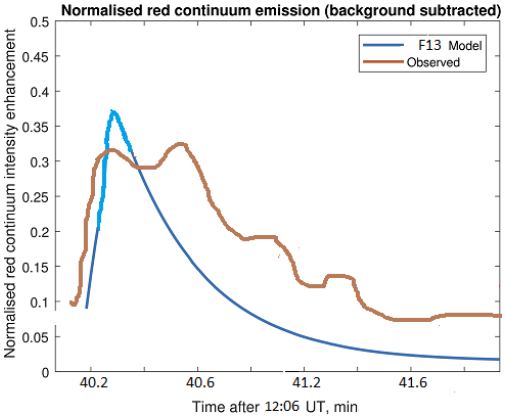

(d) Light curve 2

Fig. 6. Simulated variations of the contribution functions of Paschen continuum (white light emission) derived from a radiative hydrodynamic model heated by the moderate electrons beam, model F10, (a) and by the powerful mixed beam, model F13 (b) (see the text for more details). It is important to note the difference in three orders of magnitude between the intensities in the model (F10) and (F13) plots. The comparison of the light curve of intensity of Paschen emission was generated by a mixed beam with a spectral index of 4 and an initial energy flux of 1×10^{13} $erg/cm^2/s$ with what was measured from HMI/SDO images in WL kernel 1, coinciding with Hα kernel 1 (c), and in WL kernel 2, coinciding with Hα kernel 3 (d).

hydrogen emission in a flaring atmosphere, thus affecting, in turn, the intensity and duration of the Balmer and Paschen continua via the opacity of Lyman continuum (Druett & Zharkova 2019).

This logically explains a much slower decrease in the observed white light emission in the second WL kernel (Fig. 6d) compared to the first one (Fig. 6c). Moreover, it looks like in WL kernel 2 there were two beam injections following Lyα light curves, as shown in Paper 1 (Zharkov et al. 2020). This is revealed in the WL emission by a double maximum, which may explain the very extended decay of WL emission in this flaring event that has also been confirmed by other observers (see, e.g. Romano et al. 2018).

4. Hydrodynamic response of the solar interior

4.1. Theory of acoustic response of the solar interior

Hydrodynamic shocks from the flaring atmosphere discussed above in Section 2 can be used as the initial condition for another hydrodynamic model developed for acoustic wave propagation in the solar interior (Zharkov 2013). Since the atmospheric hydrodynamic shocks can travel in the solar interior with supersonic velocities, they generate acoustic (or magneto-acoustic) waves owing to another hydrodynamic response, this time of the solar interior to the shock. As is shown by Zharkov (2013), the vertical shock perturbation moving with a supersonic velocity can generate the set of multiple acoustic waves, from which only the waves with the phase speed exceeding a certain threshold (see Equation 5.8 in Zharkov 2013) can produce observable acoustic waves. Using Lamb's acoustic cut-off frequency and the sound speed profile from a solar interior mode, the acoustic wave equation can then be solved either analytically for a polytrope model of the solar interior (Zharkov 2013) or numerically (Shelyag et al. 2009) for Christensen-Dalsgaard's model S (Christensen-Dalsgaard et al. 1996), as described by Macrae et al. (2018).

The source of the deposited impulse, depending on its properties, generates a family of rays that provides the solution to the ray equations in phase space and defines the generated wave front. The acoustic wave packets generated by the initial shock are contained in a closed cone around the velocity vector propagating in the solar interior and being reflected back to the solar surface, reflection from which secures their detection from Doppler observations on the surface as evaluated for a polytrope model Zharkov (2013). Because the source generating the waves is located in the interior, the first ray out of all of the waves generated by the source to reach its upper turning point defines the minimal distance where the ripple is formed. An individual ray, which is characterised by a constant frequency, ω, and a horizontal wavenumber, k_h, initialised at a given depth, generally have two, upper and lower, turning points (see Fig. 1 in Zharkov 2013). The first upper turning point along the ray defines its first surface appearance (as a first ripple); the lower turning point indicates where the wave changes its direction of its motion in the interior by being reflected back to the surface. Then the propagating ripples correspond to a sequence of the source-generated acoustic rays from the packet reaching consequently their upper turning points (for more details see also Macrae et al. 2018).

For a near-surface source, the first surface appearance of a reflected wave, or the minimal distance from the deposition point, can be approximated by the ray's skip distance, Δ. For the polytrope model of the solar interior (Zharkov 2013), the minimal skip distance, Δ, or the distance from the point of the initial impulse deposition to the first ripple occurrence (see Appendix A1 in Zharkov 2013) is as follows:

$$\Delta(k_h, \omega) = (\omega)^2 \pi m/(k_h)^2 g = (V_{ph})^2 \pi m/g, \quad (1)$$

where g is the gravitational constant, $g = 2.67{\times}10^{-4}$ Mm s^{-2}, m is the polytrope index, and $V_{ph} = w/k_h$ is the horizontal speed of wave propagation.

In this case, the rays are generated with varying frequencies above the acoustic cut-off frequency ω_{ac} at the source depth (Zharkov 2013; Macrae et al. 2018). The observations of high-frequency waves are also limited by the Nyquist frequency, ω_N, of a given instrument (11.11 mHz for HMI/SDO) and the cadence of the series, meaning that the acoustic waves with a frequency above the Nyquist frequency may not be observed.

Hence, a threshold for the minimal phase speed, v_{ph}^{min}, defining the condition for registering the first ripples on the surface by the following relation (see Equation (5.8) in paper Zharkov 2013)) can be written as:

$$v_{ph}^{min} = \frac{vc}{\sqrt{(1 - \frac{\omega_{ac}^2}{\omega_N^2})v^2 - c^2}}, \quad (2)$$

where c is the sound velocity and v is the acoustic wave velocity. The propagation of the surface ripples from a near-surface source can be determined by the phase speed of acoustic waves (Zharkov 2013); the minimal skip distance, Δ, can be estimated from Eq. (1) after a substitution of the minimal phase speed given in Eq. (2). The minimal skip distance is where these acoustic waves are reflected by the surface (the upper turning point) and observed as surface ripples.

Therefore, in order to interpret the observed seismic responses for this flare, we need to establish the following points: 1) what the depth was in the solar interior where the atmospheric shock is deposited; 2) what the average velocity of the shock was; 3) how long this velocity exceeded the local sound speed in the solar interior; 4) how deep the generated acoustic waves propagate into the solar interior, or how deep their lower turning points were; 5) with what speed the acoustic waves travel back to the surface after their reflection in the lower turning point; 6) the distance from the flare location to the upper turning point; and 7) the height of the ripples in the upper turning point, where the waves are reflected from the photosphere back to the solar interior. The answers to these points will define whether these acoustic waves are detectable and how they are detectable, either as ripples or as holographic images only.

4.2. Sunquake properties probed by the acoustic response models

Hydrodynamic modelling in a flaring atmosphere is discussed in Section 2.4. These beam-generated shocks entering the sub-

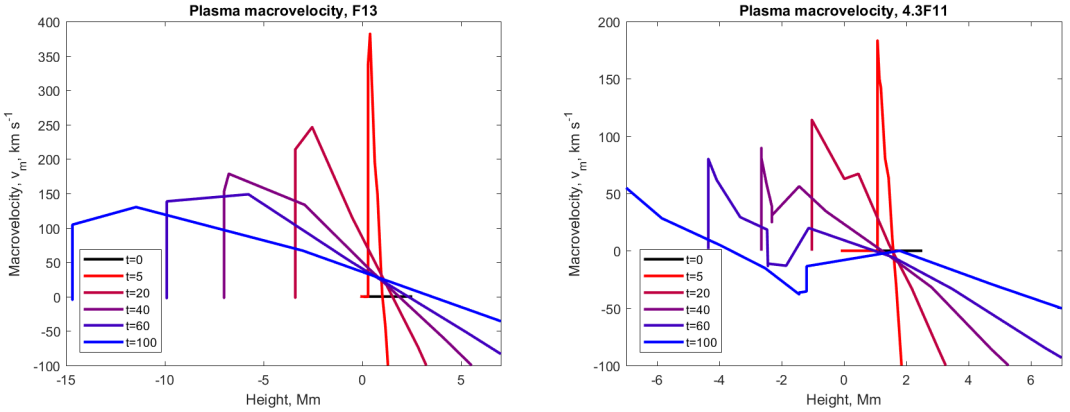

(a) Shock velocities versus the QS linear depths

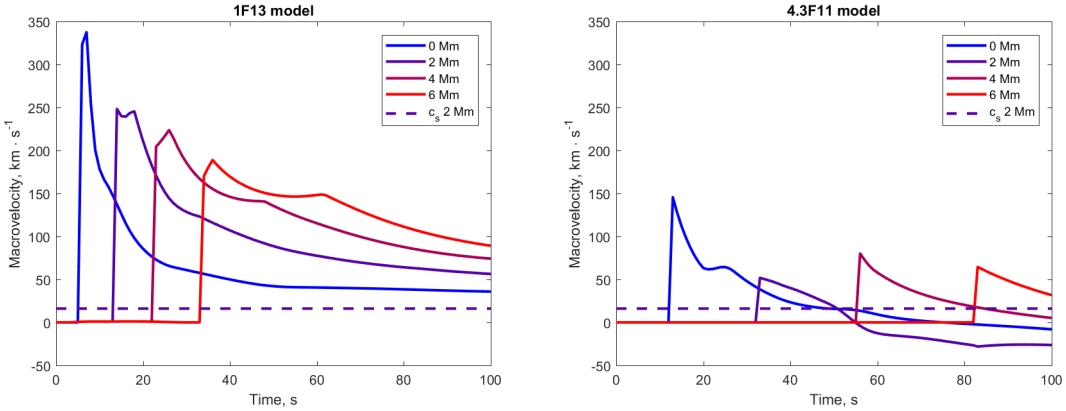

(b) Shock velocities versus time after beam onset

Fig. 7. Velocity profiles of the simulated hydrodynamic shocks in seismic event 2 of the 6 September 2017 flare (left column) and in seismic event of the 6 September 2011 flare (right column) are plotted versus the linear depths under the QS photosphere for different times after beam injection (top row) and versus the time after the beam onset for different linear depths in the solar interior under the QS photosphere (bottom row). Zero in the X-axis indicates the position of the QS photosphere, the negative numbers indicate the depth under the photosphere (see text for details). The solid black line in (a) represents the sound speed in the photosphere.

photospheric layers at a supersonic speed, as shown in Fig. 7, can generate acoustic waves (Zharkov 2013), which can be seen on the solar surface or photosphere. The acoustic waves that were generated in the interior are determined by the interior plasma properties at specific depths (e.g. sound speed, acoustic cut-off frequency) as well as by the shock velocity and its angle of shock propagation towards the normal (vertical) line to the surface.

4.2.1. Observed properties of the sunquakes

Here, we summarise the expected shock parameters associated with the detected seismic sources as follows. The three sunquakes (SQs) 1, 2, and 3, reported in Paper 1 appear at 11:55:37 UT during flaring event 1. According to the shape of the Hα-line profile in kernel 1 observed in this location, the speed that developed by ripples in seismic source 1 can be referred to as the shock induced by a strong electron or mixed beam with an energy flux of about $(6-8)\times10^{12}$ $erg\cdot cm^{-2}s^{-1}$. Whereas, for SQs 2 and 3, as concluded from the shape of the Hα line profiles and the speed of the ripples, one has to assume the shocks were induced by very powerful mixed beams with the initial energy flux of $(8-12)\times10^{12}$ $erg\cdot cm^{-2}s^{-1}$. All three SQs were detected with the holography method and time-distance diagrams.

The first signs of a ridge in the TD diagram for SQ1 appear 20-25 minutes after the flaring event 1 onset in HXR and Ly-α emission. Also, the angle of shock deposition is about -$(0-10)^\circ$ from the local vertical according to the directional holography image. The ripples generated by the shock in seismic source 1 approach the distance of 120 Mm with a velocity of 48 km/s. Seismic source 3 has a faster phase speed for the propagation of ripples because its ridge is sharper and approaches a distance that is 120 Mm faster with a speed of 51 km/s.

The strongest sunquake, SQ2, which occurred simultaneously with gamma-ray emission and Hα kernel 2, as reported in Paper 1, is well detected in the TD diagram with two ridges revealing for the first time the observations of the first and second bounces (upper turning points) of acoustic waves from the solar surface. The TD diagram for seismic source 2 shows an initial phase velocity for the ripples on the photosphere of 35 km/s; it approaches 53 km/s at the edge of the 120 Mm data cube. The

first bounce occurring at 11:55:37 UT at 5-10 Mm from the flaring event location, where the first ripples were observed, is closer than any other sunquakes that have been observed before; this has also been noted by other authors (Zhao & Chen 2018; Sharykin & Kosovichev 2018).

The HD simulations for the F13 model show that downward macrovelocity of the shock (see Fig.7, left column plots) for the conditions close to SQs 1-3 approaches 380 km/s at the maximum flux of the injected beam, while the average velocity during the first 50 seconds is about 180-200 km/s. The plasma density of the shock induced by the mixed beam with the given initial energy flux was about $(2-6)\times10^{13}\ cm^{-3}$. For comparison purposes, the conditions of a shock produced by the electron beam with the initial energy flux of $4.3\cdot10^{11}\ erg\cdot cm^{-2}s^{-1}$, which was derived for the flare of 6 September 2011 (Macrae et al. 2018), is presented in Fig.7 (right column plots). The shock induced by the less intense beam starts after the beam onset, reaching after 5 seconds the velocities of 250 km/s and propagates with the average velocity over 100 seconds not exceeding 120-150 km/s. The ripples induced by the flare of 2011 were much smaller than in the flare of 2017; as such, the ridge in the TD diagram in the flare of 2011 was even missed until Macrae et al. (2018) managed to apply the improved holography and TD techniques, allowing the authors to detect the missing sunquake.

The shocks generated by a mixed beam shown in Fig. 2c (left plot) are presented versus a linear depth of the quiet Sun (a) and time (b) (see Fig. 7, left column), while the shocks deposited by an electron beam are shown in Fig. 7 (right column). It can be noted that the shocks generated by the electron beam were first deposited above the solar surface and only later propagated with a supersonic velocity into the solar interior to depths above 500 km. Since the shocks did not travel a very long distance in the interior, no intense acoustic waves were produced. Therefore, the ridge that these acoustic waves produced in the TD diagram is not very deep, explaining why it was missed initially.

Whereas, the shock produced by the mixed beam shown in Fig. 7 (left column) is deposited within the very first few seconds in the solar interior with a supersonic speed. The hydrodynamic shock that formed in a flaring atmosphere enters the solar interior (crosses the linear depth of zero) above the local sound speed, with the vertical velocities of $v(z_s) = 380\ \mathrm{km\cdot s^{-1}}$ at $z_s = 100\ \mathrm{km\ s^{-1}}$ (Fig. 7a). The density of the shock should be $(1-3)\times10^{13}\ cm^{-3}$. The macrovelocities of a downward moving hydrodynamic shock reach 280 $\mathrm{kms^{-1}}$ at 5 s, then they slowly reduce to 175 at 50 s and approach 100 km/s at 100 s, so the average macrovelocity is about 180-200 $\mathrm{kms^{-1}}$ (see Fig. 7, left column). These downward velocities were complied well with those derived from Hα kernels 1 and 2, which were detected in the locations of seismic sources 1 and 2 for flaring event 1.

The depth of deposition of this shock in these events starts from the surface, or quiet sun photosphere, and moves down to 1000 km in depth in the interior. The plasma density in the shock is about $(5-6)\times10^{13}\ cm^{-3}$. Thus, the shock is capable of producing intense acoustic waves for a rather long time while travelling inside this interior (for comparison purposes, see the curves for different times in Fig. 7a.) Hence, the shock that was produced by the mixed beam caused a very deep ridge for the first bounce. And because the first set of acoustic waves was very intense, they had enough energy to travel to the interior, be reflected from it back to the surface following the Fermat principle, and travel to the solar surface again to become bounced back by the photosphere at the second upper turning point, as the theory predicts. Only a very intense mixed beam can produce a phenomenon similar to what was observed for the first time for the flare from 6 September 2017 (Zharkov et al. 2020).

The difference in the velocities of ripples at the edge of the dataset of 120 Mm in sunquakes 1, 2, and 3 explains a slight difference in the real flux of the mixed beams, which generated the shock in SQ1 (the lowest initial energy flux, SQ3 (medium flux), and SQ2 (the strongest initial energy flux). Also, the fact that a ridge appears in SQ2 about 10 minutes after the event onset, or at 5-10 Mm from the location of the flaring event 1 onset, indicates that the shock in SQ2 was deposited under a larger angle to the local vertical, which from the directional holography is found to be of -30°. The directional holographic image for SQ3 also indicates the inclination of the shock at about +30° from the vertical to the surface. We note that SQ1 is found to have the shock deposited closely along the local vertical under an angle of $-(0-10)°$.

The most southern seismic source 4 and middle seismic source 5 appear between 12:04 -12:07 UT, according to the Lyα light curve with FE2 starting with Hα kernel 3 at 12:06:48 UT. We do not have any high energy observations besides a UV light curve in the Lyα line. Hence, the energy flux of a beam causing the shocks in these two seismic events is a big question that has yet to be answered. However, it looks like there was a repeated injection of a strong electron beam, which occurred in the same location and 10 minutes after the injection of the first mixed beam. This injection likely caused another strong hydrodynamic shock and led to a potential (repeated) seismic source 5. Hence, in flaring event 2, there was another Hα line kernel 3 with a large redshift, which was detected in the same location as seismic source 2.

By comparing the line profile observed in Hα kernel 3, we managed to derive that Hα line profile can be produced in a flaring atmosphere heated by a mixed beam with an initial energy flux that is close to $(6-8)\times10^{12}\ erg/cm^2/s$ and a spectral index that is 4. From the simulated hydrodynamic model, we derived that the density of the shock should be $(1-3)\times10^{13}\ cm^{-3}$ and the shock macrovelocity would be slightly lower than in source 2, reaching 320 $\mathrm{kms^{-1}}$ at 5-10 sec and dropping to 100 at 50-60 s, with the average velocity of 120-140 $\mathrm{kms^{-1}}$. The shock starts above the surface and propagates as a shock down to 500-1000 km below the surface, and the angle of deposition is about +30° from the vertical as derived from a directional holography approach.

It is likely that the ripples generated by this hypothetical seismic source 5 interfere with the ripples from seismic source 2, which were generated just 10 minutes before in the same location. These acoustic waves can have a resonant interference, which was once suggested for the similar seismic events seen in Ca II dopplergrams by Hinode (Kosovichev 2011), thus producing the unusual seismic waves observed in Ca II emission in

the chromosphere for the 6 September 2017 flare (Quinn et al. 2019).

For modelling of acoustic-wave propagation, the Christensen-Dalsgaard Model C (Christensen-Dalsgaard et al. 1996) was used with the profiles of the acoustic cutoff frequency and sound speed in this model shown in Macrae et al. (2018). Therefore, the acoustic cut-off frequency, $\omega_{ac}/(2\pi)$, and sound speed, c, at depths below the surface of less than 1000 km are accepted to be equal to 9.9 mHz and 8.4 km s^{-1}, respectively. In addition, in the simulations for different seismic sources, we introduced inclinations of ±30° to the local vertical of the direction of a deposited hydrodynamic shock.

4.2.2. Simulated acoustic waves versus observations

The propagation of the acoustic waves (or rays) generated by a supersonic source moving with a velocity of 120 km s^{-1} under an angle of −10° to the vertical (seismic source 1) is presented in Fig. 8, with an average velocity of 150 km s^{-1} under an angle of +30°, presented in Fig. 9 and with an average velocity of 200 km s^{-1} at a surface depth of z_s = 0 km (as in seismic source 2) under the angle of -30° are shown, in Fig. 10. The abscissa defines a horizontal distance on the solar surface in Mm of the ripple propagation about the location of a deposition of supersonic disturbance (shock) and the ordinate shows a propagation depth, z, under the photosphere of the generated rays and wavefronts at different times for the wave vectors located in the same plane as the velocity, that is, if $\phi = 0$ (in notation of Section 5.2 of Zharkov 2013).

The acoustic wave simulation for the conditions of seismic source 1 show (see Fig. 8) that the rays in the first model deposited nearly along the local vertical have a propagation of the waves in the interior (left plot) until the first ripple is observed at 15-20 Mm from the location 20-25 minutes after the shock deposition (right plot). Since the rays move in the interior with a speed exceeding the local sound speed, these waves at frequencies above the acoustic cut-off can escape the solar interior when they reach a surface at the upper turning point. As we noted from the HD simulations of the shock deposition (Fig. 7a, right plot) in this source, the shock goes under the photosphere 10 s after the event onset. Then after 20 minutes, the rays in the model simulations shown in Fig. 8 reach the first upper turning point at the surface in the photosphere where they produce the first ripples on the surface before they turn back towards the interior.

For a shock deposition to be applicable for seismic event 3, the appearance of the ridge is seen earlier at 10 seconds after the acoustic wave onset and at the distance of 8-10 Mm (Fig. 9). This happens because the deposition angle of the shock in source 3 was not zero but +30° and, for example, the rays on the left side of the deposition point do not travel as deep into the interior and thus reach the surface faster than in source 1 at 16.83 minutes. The rays on the right-hand side in source 3 travel deep enough, but they produce the ripples too far away from the source, outside the data cube of 120 Mm used by HMI.

Whereas, for the seismic model for SQ2, which is shown in Fig. 10, the shock caused by the mixed beam is deposited just at the surface and propagates much deeper into the interior with a supersonic speed (as shown in the video attached with the paper in the supplementary materials) so that the acoustic wave produced by this shock moves into a much deeper interior. However, since this wave packet travels under the angle -30°, it produces the acoustic rays in the shortest path, on the right-hand side, and in the longest one, on the left-hand side. Because the acoustic rays started from the surface and travel much deeper into the interior, they gain a much higher velocity before reaching the lower turning points than the rays with a shock deposited well above the surface and, thus, travelling with supersonic velocities in the interior pretty limited time and losing more energy. The rays which travel to deeper layers when reflected back to the surface by the Fermat principle (Zharkov 2013) have much higher velocities and, when they approach the photosphere in the upper turning point, they create larger ripples, which can be easily detected in the time-distance diagrams as reported for seismic source 2, as shown in Paper 1.

Also, because in SQ2 the shock is deposited at an angle of -30° from the local vertical, the first upper turning point is seen very quickly at about 8-10 minutes after the impact at the distance approaching 5 Mm from the source. This is in close agreement with the skip distance derived from TD diagrams and is similar to the results reported by Zhao & Chen (2018). Moreover, for this seismic event, the velocities of the rays reflected back to the interior after they produced the first ripples are still high. This is reproduced in the model acoustic waves shown in Fig. 10, where the first points of reflection from the surface are observed 15 minutes after the deposition time starting from a distance of 2 Mm and they are very well seen within 20 minutes from the distance of 3 Mm.

Since the shock deposited in the atmosphere with SQ2 was very strong, these reflected rays are capable of traveling to the interior and become reflected back again to return to the surface. Given the high ratio of the source-to-local sound speed, the wave-packet that is generated at this depth is expected to be rather wide because only the rays with $\theta > 86^\circ$ become evanescent for $\phi = 180^\circ$. Hence, as result, these acoustic waves are rather strong at producing the second lower and upper turning points, leading to a second bounce seen in the TD diagram for this seismic source reported in Paper 1 (Zharkov et al. 2020). Indeed, these second bounce waves are seen in the simulated acoustic waves, which can be seen in Fig. 10 (the top right end of the wave set marked by the blue curve), showing the second bounce waves to start at 5 Mm in the model set at 15 minutes and at 7 Mm in the set at 20 minutes.

When the shocks in any models travel deeper into the interior, their velocity decreases while the sound speed grows, making the wave packets generated at these larger depths narrower and with lower frequencies. For seismic events 2 and 3, the fact that there are observed signatures at low frequencies of 3 mHz indicates that the shocks generated in these events must have travelled to at least 600-1000 km below the surface, which is in agreement with the modelling of hydrodynamics of the shocks in flaring atmosphere shown in Fig. 7, left column. Whereas, seismic event 1 was likely generated in a more shal-

low region below the surface and, thus, does not reveal lower frequency acoustic waves.

Hence, in the summary, one can note that the acoustic waves (rays) generated by hydrodynamic shocks induced by a mixed beam (MB) in the largest sunquake (source 2) are found to travel much faster and to deposit their momentum much deeper in the solar interior, thus producing type 1 acoustic waves with double ridges: a very visible first bounce (main) ridge and a detectable second-bounce ridge. The shocks deposited by an electron beam (EB) produce type 2 acoustic waves with a weaker single ridge, as seen in seismic sources 1 and 3. As a result, these type 1 acoustic waves reach the first lower turning point in deeper interior depths, thus, gaining higher velocities compared to the type 2 acoustic waves, which are generated in the shallow interior beneath the flare like in seismic source 1 of this flare of 6 September 2017 or in the nearly missed seismic source of the 6 September 2011 flare. These type 1 acoustic waves approach higher velocities in the interior, with which they travel back to the surface in the photosphere to their first upper turning point (or first bounce), creating ripples while being reflected back to the interior. The reflected wave energy is lower than the original one but still sufficient to travel again to the less deep interior and to return back for a second bounce, creating secondary, slower, ripples.

From a directional holography analysis, the different seismic sources are found to have a different directivity, or angle, from the vertical for a momentum deposition. The type 1 acoustic waves that were simulated in seismic source 2 for a momentum deposited at an angle of -30° from the vertical demonstrate the occurrence of well detectable ripples at the photosphere seen a few minutes after the impact at a distance approaching 5-10 Mm from the source, which is in close agreement with the distance derived from the TD diagram.

The other two sources show the characteristics of the rays to be consistent with being produced by shocks generated by electron beams and deposited at angles (0-10)° (source 1) and +30° (source 3) to the local vertical, which propagate beneath the surface but not too deep into the interior, which is contrary to type 1 acoustic waves in seismic source 2. These weaker shocks create weaker acoustic waves at shallower depths of the interior, which are reflected by the interior to the solar surface (at lower turning points) with smaller velocities. When these acoustic waves reach the solar surface (photosphere) and become reflected by it (at the upper turning point), they create much smaller ripples in the photosphere, which can only be picked up as regular features by the holographic approach.

5. Discussion and conclusions

In this paper, we attempt to understand the complex appearance of two flaring events in the flare of 6 September 2017, which were observed with a different degree of coverage in time and space by multi-wavelength instruments. During the flare, there were four locations linked to footpoints of three magnetic ropes where four (5) sunquakes were identified with acoustic holography (4) and time-distance diagram (3) techniques. Also, three Hα kernels were observed: the two during FE1 with strongly redshifted line profiles co-spatial with two detected sunquakes (SQ1 and SQ2) and the one kernel during FE2 linked to the alleged SQ5 that occurred during FE2 in the SQ2 location, 10 minutes after FE1. The locations of sunquakes 1-3 of FE1 were overlapped with strong EUV emission, reflecting explosive evaporation of the chromospheric plasma into the flaring corona in these locations observed by EIS/Hinode, whose field of view could not see the SQ4 in the southern part of the active region. There was also the location of SQ2 where we derived two light curves of white light emission for FE1 and FE2.

For the identification of magnetic field topology and footpoints where all of these flaring events can occur, we used the NLFFF restoration of the magnetic field and MHD simulations based on the restored magnetic field, which helped us to obtain the magnetic structure of the active region where flaring events occurred and to link the footpoints of these magnetic ropes to the locations of sunquakes, Hα line kernels, EUV emission with large blueshifts, and WL brightening. In practical terms, the area of flaring footpoints were defined from the area of Hα emission kernels or from the area where TD diagrams that allowed one to evaluate the initial energy fluxes of the particle beams heating these flaring atmospheres using the parameters derived from the KONUS HXR and GR emission in FE1 as a basis. For FE2, we only detected Hα kernel 3 and white light emission, thus solely allowing us to speculate about possible conditions of atmosphere heating based on the good fit to the simulated and observed Hα line profiles and light curves of WL emission.

In order to simulate the Hα line profiles for the conditions relevant for the observed kernels, we produced the model flaring atmospheres heated by intense mixed beams which were likely present in the flare of 6 September 2017 as per KONUS/WIND observations with the initial fluxes of $(6-12)\cdot 10^{12}\ erg\cdot cm^{-2}s^{-1}$ and a spectral index of 4. Additionally, we compared the emission produced in the current hydrodynamic models with the emission in another flare of 6 September 2011, which was produced by the electron beam with an initial flux of $4.3\cdot 10^{11}\ erg\cdot cm^{-2}s^{-1}$.

These models were used to explain the observations of Hα line profiles reasonably well with CRISP/SST and white light emission from HMI/SDO with the simulated emission of Balmer line and Paschen continuum, which is seen in white light. These models also helped us to explain upward velocities of the observed EUV spectrograms and their close co-location with sunquakes 1, 2, and 3 accompanied by the observed dimming and large redshifts of Hα line emission at flaring events 1 and 2. We demonstrated with the simulations that WL emission in FE1 and FE2 can only be produced by the same particle beams that produce all other observational signatures because they induce a strong over-ionisation of hydrogen in the chromosphere and photosphere.

Based on the parameters of the seismic events derived from observations, we applied a combination of two hydrodynamic models: one for a flaring atmosphere heating by a mixed beam and the second one for the production of acoustic waves in the solar interior by the shock coming from the flaring atmosphere for three seismic sources 1, 2, and 3. In order to evaluate the role of magnitude of the shocks produced in a flaring atmosphere by a very powerful mixed beam and a less powerful

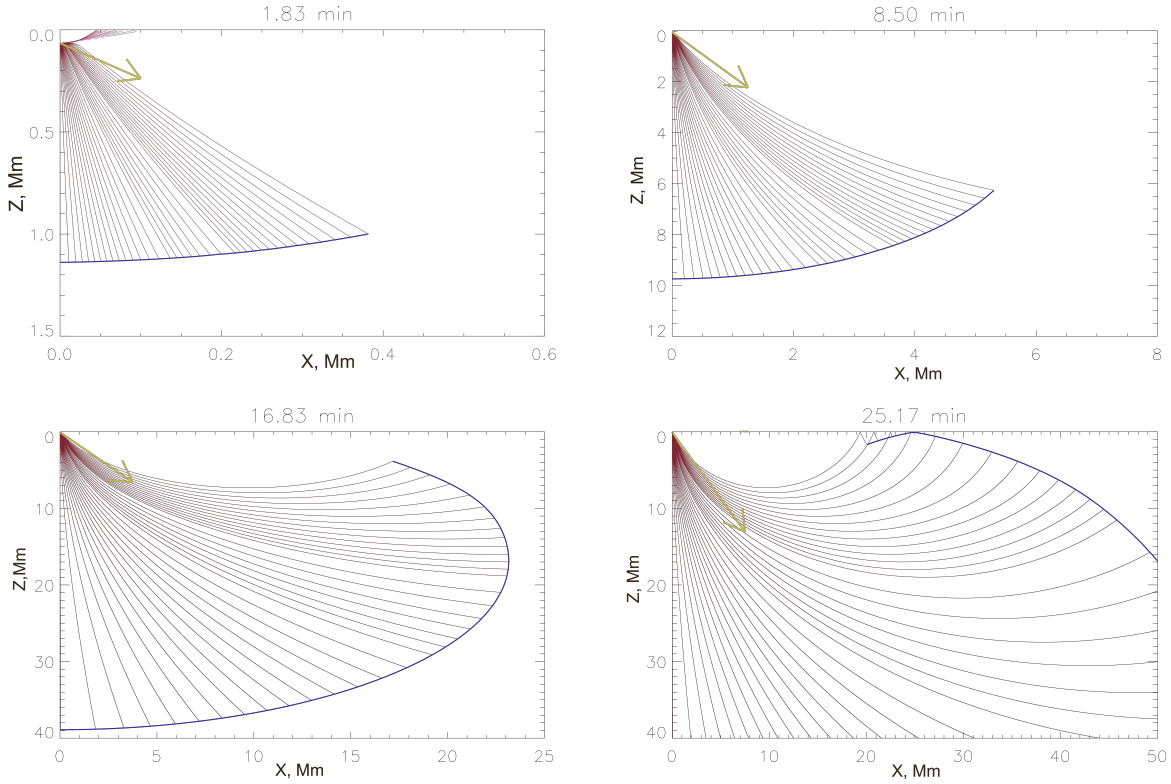

Fig. 8. Individual acoustic rays generated at the depth of 1 km in the solar interior and travelling along the Z direction to the bottom of the plot by a moving supersonic source, v = 120 km s^{-1}, depositing a momentum below the photosphere (the origin) under a -10 ° angle from the local vertical for the times after shock onset. This is shown above the plots and is similar to what was observed in seismic source 1. The rays were computed numerically for the parameters extracted from model S (Christensen-Dalsgaard et al. 1996). The rays are colour-coded in the range of 9-15 mHz with 9 corresponding to the darkest shade; Z is depth in the solar interior; the photosphere is denoted by Z=0; and the X-axis denotes a distance on the surface in Mm from the point of the momentum deposition. The mustard arrow shows the direction of the wave propagation. The points of the ray reflection from the photosphere seen in the top right corner at 25:17 min from the shock deposition time are observed as ripples on the surface, or a sunquake, which are propagating from the central point of the momentum deposition in the flaring event outwards to all the directions.

electron beam on the resulting seismic signatures, we demonstrated the difference between the deposition depths, velocities, and duration of the propagation with supersonic velocities of these shocks in the solar interior, where they are capable of generating acoustic waves. These models provide the plausible quantitative link between the hydrodynamic shocks in flaring atmospheres and the seismic signatures induced by another hydrodynamic response of the solar interior beneath the flaring events to the deposition of these hydrodynamic shocks.

The simulations show that for the plasma heated by a mixed beam, the explosive evaporation starts from the very first seconds with high macrovelocities of 100 km·s^{-1}, which was simulated in the lower flaring corona (Fig.2c, left column), and approaching the velocities of 400-500 km·s^{-1} 5 seconds after the beam onset, which later, at 30-50 s after the event onset, become reduced to 250 km/s. However, observations by Fe XXIII line only started 10-15 seconds after the beam onset, when the beam was off and the plasma had cooled off to the temperature of ten millions of K required to see this emission. The spectrograms of the Fe XXIII 263.76 Å line for FE1 in footpoint FP3 of SQ1 reveal large upward velocities of 300-350 kms^{-1}, similar to the simulated velocities in the hydrodynamic model of the flaring atmosphere heated by the mixed beam. For SQ 2, the blueshift in the line of Fe XXIII 263.76 Å, indicating the macrovelocity of explosive evaporation, exceeds 400 km/s much faster than in the atmosphere with SQ 1, indicating a stronger shock in the location of SQ 2. This likely led to the additional ridge in the time distance diagram of sunquake 2, constituting a double bounce of acoustic waves.

These upward motions are combined with the downflows of > 100-200 kms^{-1}, which are seen in the He II spectrograms associated with SQ1 and SQ2. However, the EIS observations in He II 256 Å in the locations of SQ1 and SQ2 appear 30 s after the onset of FE1, confirming that the temperature of flaring atmosphere reached the magnitudes of raditaive temperature of the He II line. To this point, this also indicates that the starting time of SQ1 and SQ2 is 20-25 s earlier than the redshift in the He II line. However, the redshift in the He II line exists for about a minute, which is close to what was predicted by hydrodynamic simulations. It is remarkable that after a minute or so these downflows are followed by upflows with magnitudes of macrovelocities that are close to those predicted by the hydrodynamic (HD) simulations carried out for heating by a mixed beam in SQ1 and SQ2.

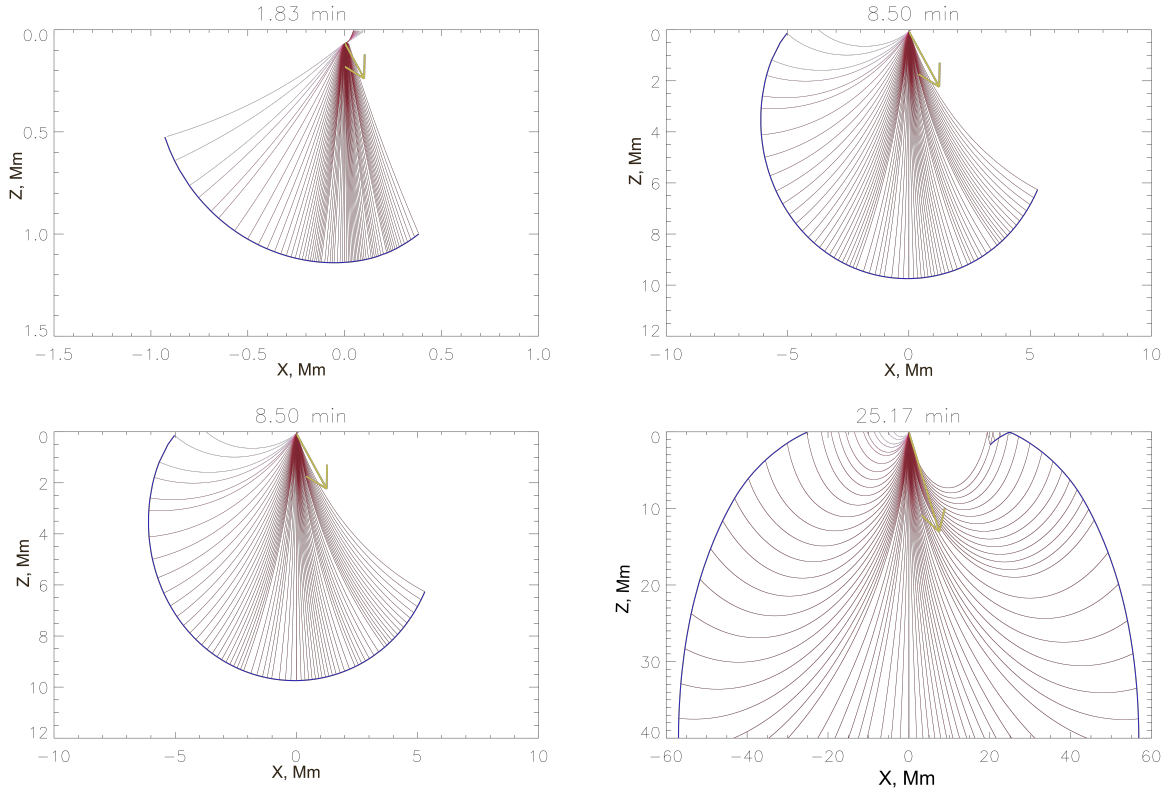

Fig. 9. Individual acoustic rays generated at the depth of 45 km in the interior and travelling to the bottom of the plot by a moving supersonic source with a velocity of $v = 150\,\mathrm{km\,s^{-1}}$, depositing a momentum below the photosphere under a +30 ° angle from the local vertical for the times after the shock deposition shown above the plots. We note that Z is the depth in the solar interior, the photosphere is denoted by Z=0, and the X-axis denotes a distance on the surface in Mm from the point of the momentum deposition. The mustard arrow shows the direction of the wave propagation. The points of ray reflection from the photosphere seen in the top left corner 8:50 min after the shock deposition are observed as ripples on the surface, or a sunquake, which are propagating from the central point of the momentum deposition in the flaring event outwards to all the directions.

It can be observed that the upward macrovelocities in the HD model approach 300-400 km/s, which is similar to those measured by the EIS instrument for the location of seismic source 1. At the same time, the downward motion modelled for this event also reaches the macrovelocity of 300 km/s, 5 seconds after the beam onset, and is then reduced to 150-200 km/s for the next few minutes. These redshifts are close to what was measured in Hα kernel 1, which was likely to be redshifted by 3-4 Å, so only the blue wing of the line has been observed. At the same time, the He II 256 Å spectrograms in the location of the largest sunquake 2 reveal that similarly to the hydrodynamic simulations, the redshifts approaching 380 $\mathrm{kms^{-1}}$ drop to 250-300 km/s 15-20 seconds after the beam offset. The observed He II redshifts in an excess of 250 $\mathrm{kms^{-1}}$ are well-correlated with those observed in the locations of the largest sunquake 2. This redshift also corresponds to the strong one of 5-6 |AA, which was measured in Hα kernel 2, where only the far blue wing is observed with the intensity lower than that of Hα kernel 1. The simulated and measured blueshifts in SQ2 and the Fe XXIII line start from 150 km/s at 1 second approaching 400 km/s within a short timescale of 15-30 seconds.

We also investigate the scenario of acoustic wave generation by hydrodynamic shocks propagating for up to 50-60 seconds in the solar interior with supersonic velocities and generating acoustic waves above the acoustic cutoff frequency. During the flare of 6 September 2017, the shocks in SQs 1-3 were deposited beneath the solar surface and travelled much longer in the interior, producing acoustic waves compared to the shock generated in the flare of 6 September 2011 reported earlier (Macrae et al. 2018). This difference in the shock deposition depths explains the clear ridges observed in the time-distance diagrams of SQ1, SQ2, and SQ3 in the 6 September 2017 flare versus the rather weak ridge observed in the 2011 flare.

The acoustic waves (rays) generated by the HD shock induced by a mixed beam (MB) in the largest sunquake (SQ 2) are found to travel much faster and to deposit their momentum much deeper in the solar interior, producing type 1 acoustic waves with double ridges: a very visible main ridge and a detectable second-bounce ridge seen in the 6 September 2017 flare. The shocks deposited by an electron beam (EB) produce type 2 acoustic waves with a weaker single ridge, as is seen in the seismic source of 6 September 2011 flare. As a result, these type 1 acoustic waves reach the first lower turning point in deeper interior depths, thus, gaining higher velocities compared to the type 2 waves. These type 1 acoustic waves approach higher velocities in the interior, with which they travel back to the surface in the photosphere to their first upper turning point

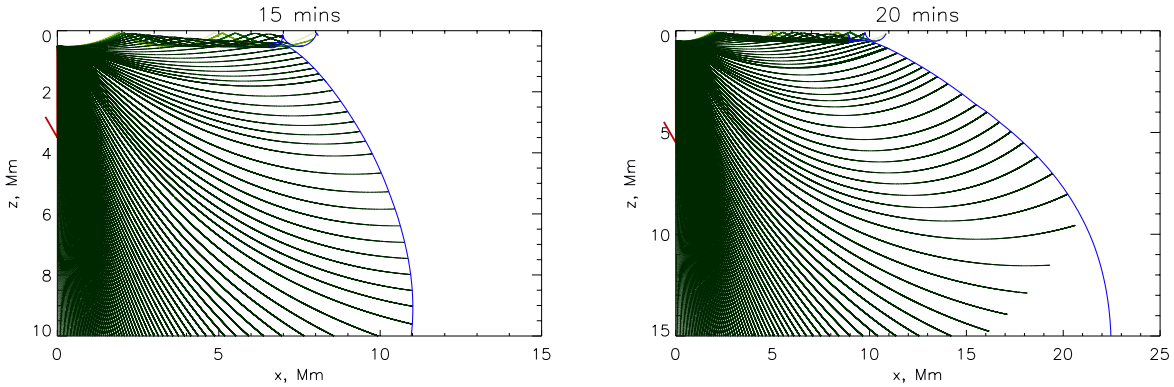

Fig. 10. Individual acoustic rays travelling to the bottom of the plot generated in the interior by a moving supersonic source with an average speed of $v = 200\,\mathrm{km\,s^{-1}}$ as in seismic source 2 at the times denoted on the top of each panel. The shock is inclined by -30° to the local vertical. Note that *Z* is the depth in the solar interior, the photosphere is denoted by Z=0, and the X-axis denotes a distance on the surface in Mm from the point of the momentum deposition. The mustard arrow shows the direction of the wave propagation. The points of reflection from the surface, or ripples of the first bounce, are well observed 15 minutes after the deposition time, starting from a distance of 2-3 Mm (on the right), and they are very well seen within 20 minutes at a distance starting from 3-4 Mm. The second bounce waves appear at 5 Mm within 15 minutes after the shock deposition and at 7 Mm within 20 minutes (see the top far end of the wave set marked by the blue curve). Note that a video animation of these acoustic waves is presented in the supplementary materials, which shows propagation of the generated acoustic waves with the first and second bounces, as observed in seismic source 2.

(or first bounce), creating ripples while being reflected back to the interior. The reflected wave energy is lower than the original one, but it is sufficient to travel to the less deep interior and to return back again to the surface for a second bounce creating the secondary, slower, ripples.

The type 1 acoustic waves simulated in seismic source 2 for a momentum deposited at an angle of -30° from the vertical and travelling rather deep into the solar interior demonstrate the occurrence of strong acoustic waves in the interior. These waves become reflected from the solar surface during the first bounce (or the first upper turning point), thus forming well detectable ripples at the photosphere a few minutes after the impact at a distance approaching 5-10 Mm from the start location of SQ2 that is in close agreement with the distance and time derived from the TD diagram. There are also the second bounce acoustic waves, which are seen in the simulated wave packets occurring at the second upper turning point at the photosphere, showing them to start at 5 Mm in the model set at 15 minutes and at 7 Mm in the model set at 20 minutes, which are also close to the parameters derived from the TD diagram for seismic source 2. The two other seismic sources SQ1 and SQ3 show the acoustic waves whose characteristics are consistent with those being produced by shocks generated by slightly weaker mixed beams and deposited at angles of -$(0-10)$° (seismic sources 1) and +30° (source 3) to the local vertical, which propagate beneath the surface but not too deep into the interior.

Hence, by combining the two hydrodynamic models, of flaring atmosphere and acoustic wave generation in the solar interior, we are able to provide the simultaneous quantitative interpretation of the three seismic events whose characteristics were also confirmed with blue and redshifts, which were derived from the combined EUV and Hα emission observed in the X9.3 flare of 6 September 2017. We show that, in spite of disparity of spatial and temporal resolution, all of the observed signatures can be logically accounted for by the complex hydrodynamic dynamic processes in the flaring atmospheres of interacting magnetic loops and the interior beneath caused by the injection of mixed beams.

References

Allred, J. C., Hawley, S. L., Abbett, W. P., & Carlsson, M. 2005, ApJ, 630, 573
Antonucci, E., Gabriel, A. H., Acton, L. W., et al. 1982, Sol. Phys., 78, 107
Aptekar, R. L., Frederiks, D. D., Golenetskii, S. V., et al. 1995, Space Sci. Rev., 71, 265
Bradshaw, S. J. & Cargill, P. J. 2006, A&A, 458, 987
Brown, J. C. 1971, Sol. Phys., 18, 489
Buitrago-Casas, J., Martinez-Oliveros, J., Lindsey, C., et al. 2015, solphys, 290, 3151
Canfield, R. C. & Gayley, K. G. 1987, ApJ, 322, 999
Christensen-Dalsgaard, J., Dappen, W., Ajukov, S. V., et al. 1996, Science, 272, 1286
Cox, D. P. & Tucker, W. H. 1969, ApJ, 157, 1157
Culhane, J. L., Harra, L. K., James, A. M., et al. 2007, Sol. Phys., 243, 19
Ding, M. D. & Fang, C. 1996, Sol. Phys., 166, 437
Dominique, M., Hochedez, J.-F., Schmutz, W., et al. 2013, Sol. Phys., 286, 21
Donea, A. 2011, Space Sci. Rev., 158, 451
Donea, A. & Lindsey, C. 2005, ApJ, 630, 1168
Donea, A.-C., Besliu-Ionescu, D., Cally, P. S., Lindsey, C., & Zharkova, V. V. 2006, Solar Physics, 239, 113
Donea, A.-C., Braun, D. C., & Lindsey, C. 1999, ApJ, 513, L143
Donea, A.-C., Lindsey, C., & Braun, D. C. 2000, Sol. Phys., 192, 321
Doschek, G. A., Kreplin, R. W., & Feldman, U. 1979, ApJ, 233, L157

Doschek, G. A., McKenzie, D. E., & Warren, H. P. 2014, ApJ, 788, 26
Druett, M., Scullion, E., Zharkova, V., et al. 2017, Nature Communications, 8, 15905
Druett, M. K. & Zharkova, V. V. 2018, A&A, 610, A68
Druett, M. K. & Zharkova, V. V. 2019, A&A, 623, A20
Duijveman, A., Somov, B. V., & Spektor, A. R. 1983, Sol. Phys., 88, 257
Fisher, G. H., Bercik, D. J., Welsch, B. T., & Hudson, H. S. 2012, Sol. Phys., 277, 59
Fisher, G. H., Canfield, R. C., & McClymont, A. N. 1985a, ApJ, 289, 434
Fisher, G. H., Canfield, R. C., & McClymont, A. N. 1985b, ApJ, 289, 425
Fisher, G. H., Canfield, R. C., & McClymont, A. N. 1985c, ApJ, 289, 414
Gordovskyy, M., Zharkova, V. V., Voitenko, Y. M., & Goossens, M. 2005, Advances in Space Research, 35, 1743
Green, L. M., Valori, G., Zuccarello, F. P., et al. 2017, ApJ, 849, 40
Hochedez, J.-F., Schmutz, W., Stockman, Y., et al. 2006, Advances in Space Research, 37, 303
Hudson, H., Fisher, G., & Welsch, B. 2008, in Astronomical Society of the Pacific Conference Series, Vol. 383, Subsurface and Atmospheric Influences on Solar Activity, ed. R. Howe, R. Komm, K. Balasubramaniam, & G. Petrie, 221
Ichimoto, K. & Kurokawa, H. 1984, Sol. Phys., 93, 105
Inoue, S., Shiota, D., Bamba, Y., & Park, S.-H. 2018, ApJ, 867, 83
Ivanov, V. V. & Serbin, V. M. 1984, Soviet Ast., 28, 405
Kaempfer, N. & Magun, A. 1983, ApJ, 274, 910
Kennedy, M. B., Milligan, R. O., Allred, J. C., Mathioudakis, M., & Keenan, F. P. 2015, A&A, 578, A72
Kobylinskii, V. A. & Zharkova, V. V. 1996, Advances in Space Research, 17, 129
Kosovichev, A. 2011, arXiv preprint arXiv:1103.1707
Kosovichev, A. G. & Zharkova, V. V. 1998, Nature, 393, 317
Kotrč, P., Procházka, O., & Heinzel, P. 2016, Sol. Phys., 291, 779
Kuridze, D., Mathioudakis, M., Simões, P. J. A., et al. 2015, ApJ, 813, 125
Kurokawa, H., Takakura, T., & Ohki, K. 1988, PASJ, 40, 357
Lemen, J. R., Title, A. M., Akin, D. J., et al. 2011, Sol. Phys., 241
Lin, R. P., Dennis, B. R., Hurford, G. J., et al. 2002, Sol. Phys., 210, 3
Lindsey, C. & Braun, D. 2000, solphys, 192, 261
Lindsey, C. & Braun, D. C. 1999, ApJ, 510, 494
Liu, C., Deng, N., Lee, J., et al. 2014, Apj, 795, 128
Lysenko, A. L., Anfinogentov, S. A., Svinkin, D. S., Frederiks, D. D., & Fleishman, G. D. 2019, ApJ, 877, 145
Macrae, C., Zharkov, S., Zharkova, V., et al. 2018, A&A, 619, A65
Martínez-Oliveros, J.-C., Hudson, H. S., Hurford, G. J., et al. 2012, ApJ, 753, L26
Matthews, S. A., Harra, L. K., Zharkov, S., & Green, L. M. 2015, ApJ, 812, 35
Matthews, S. A., Zharkov, S., & Zharkova, V. V. 2011, ApJ, 739, 71
Milligan, R. O. 2015, Sol. Phys., 290, 3399
Milligan, R. O., Kerr, G. S., Dennis, B. R., et al. 2014, ApJ, 793, 70
Polito, V., Reep, J. W., Reeves, K. K., et al. 2016, ApJ, 816, 89
Quinn, S., Reid, A., Mathioudakis, M., et al. 2019, ApJ, 881, 82
Radziszewski, K., Rudawy, P., & Phillips, K. J. H. 2011, A&A, 535, A123
Romano, P., Elmhamdi, A., Falco, M., et al. 2018, ApJ, 852, L10
Scharmer, G. B. 2006, A&A, 447, 1111
Scharmer, G. B., Dettori, P. M., Lofdahl, M. G., & Shand, M. 2003, in Society of Photo-Optical Instrumentation Engineers (SPIE) Conference Series, Vol. 4853, Innovative Telescopes and Instrumentation for Solar Astrophysics, ed. S. L. Keil & S. V. Avakyan, 370–380
Scherrer, P. H., Schou, J., Bush, R. I., et al. 2012, Sol. Phys., 275, 207
Sharykin, I. N. & Kosovichev, A. G. 2018, ApJ, 864, 86
Shelyag, S., Zharkov, S., Fedun, V., Erdélyi, R., & Thompson, M. J. 2009, A&A, 501, 735
Shmeleva, O. P. & Syrovatskii, S. I. 1973, Sol. Phys., 33, 341
Siversky, T. V. & Zharkova, V. V. 2009, Journal of Plasma Physics, 75, 619
Somov, B. V., Spektor, A. R., & Syrovatskii, S. I. 1981, Sol. Phys., 73, 145
Syrovatskii, S. I. & Shmeleva, O. P. 1972, Soviet Astronomy, 16, 273
Uchida, Y. & Hudson, H. 1972, Sol. Phys., 26, 414
Veronig, A., Vršnak, B., Temmer, M., & Hanslmeier, A. 2002, Sol. Phys., 208, 297
Woods, T. N., Lean, J. L., & Eparvier, F. G. 2006, in Proceedings of the ILWS Workshop, ed. N. Gopalswamy & A. Bhattacharyya, 145
Wuelser, J.-P. & Marti, H. 1989, ApJ, 341, 1088
Zarro, D. M., Canfield, R. C., Metcalf, T. R., & Strong, K. T. 1988, ApJ, 324, 582
Zhao, J. & Chen, R. 2018, ApJ, 860, L29
Zharkov, S. 2013, Monthly Notices of the Royal Astronomical Society, 431, 3414
Zharkov, S., Green, L., Matthews, S., & Zharkova, V. 2011b, ApJ, 741, L35
Zharkov, S., Matthews, S., Zharkova, V., et al. 2020, A&A, in press, Paper 1
Zharkov, S., Zharkova, V. V., & Matthews, S. A. 2011a, ApJ, 739, 70
Zharkova, V. & Kobylinskii, V. 1993, Sol. Phys., 143, 259
Zharkova, V. & Zharkov, S. 2007, ApJ, 664, 573
Zharkova, V. & Zharkov, S. 2015, Sol. Phys., 290, 3163
Zharkova, V. V. 2008, Sol. Phys., 251, 641
Zharkova, V. V., Arzner, K., Benz, A. O., et al. 2011, Space Sci. Rev., 159, 357
Zharkova, V. V. & Gordovskyy, M. 2006, ApJ, 651, 553
Zharkova, V. V. & Kobylinskii, V. A. 1993, Sol. Phys., 143, 259

6. Acknowledgements

The authors wish to express their deep gratitude to the anonymous referee for constructive and useful comments, from which the paper strongly benefited. The authors express their gratitude to Dr. A. Lysenko (IOFFE Institution, St. Petersburg, Russia) for offering the KONUS data with their full explanations and useful discussion. The authors acknowledge that HMI and AIA images are available by courtesy of NASA/SDO and the AIA, EVE, and HMI science teams. The Swedish 1-m Solar Telescope is operated on the island of La Palma by the Institute for Solar Physics of Stockholm University in the Spanish Observatorio del Roque de los Muchachos of the Instituto de Astrofísica de Canarias. The LYRA is a project of the Centre Spatial de Liege, the Physikalisch-Meteorologisches Observatorium Davos, and the Royal Observatory of Belgium, funded by the Belgian Federal Science Policy Office (BELSPO) and by the Swiss Bundesamt fuer Bildung und Wissenschaft. M. Druett's acknowledges the support of his research by the Swedish Research Council, grant number 2017-04099. S. Zharkov and V. Zharkova acknowledge the funding for this research provided by the U.S. Air Force grant PRJ02156. S. Matthews acknowledges a financial support from STFC via the Consolidated Grant ST/N000722/1.